Multiple-Angle Incidence Resolution Spectrometry (MAIRS): Applications in Nanoarchitectonics and Applied Physics

Nobutaka Shioya[1], Taizo Mori[1], Katsuhiko Ariga[2,3], and Takeshi Hasegawa[1]*

[1]*Institute for Chemical Research, Kyoto University, Gokasho, Uji, Kyoto 611-0011, Japan*
[2]*Research Center for Materials Nanoarchitectonics (MANA), National Institute for Materials Science, Tsukuba 305-0044, Japan*
[3]*Graduate School of Frontier Sciences, The University of Tokyo, 5-1-5 Kashiwa-no-ha Kashiwa 277-8561, Japan.*

E-mail: htakeshi@scl.kyoto-u.ac.jp, ARIGA.Katsuhiko@nims.go.jp

Abstract:

The cutting-edge thin film studies using the multiple-angle incidence resolution spectrometry (MAIRS) are introduced from the principle to forefront applications in a wide variety of research fields covering semiconductor material with respect to nanoarchitectonics. MAIRS basically reveals quantitatively optical anisotropy in thin films, which is mostly used for quantitative molecular orientation analysis of each chemical group for chemistry purposes. This works powerfully especially when the material has poor crystallinity that cannot be analyzed by X-ray diffraction analysis. As a matter of fact, MAIRS works as a role that compensates for the diffraction techniques, and the combination of MAIRS and the diffraction techniques has already established as the most powerful technique not to miss the molecular aggregation structure in thin films. In this review, in addition, another application for physics purposes is also introduced where phonon in thin films is discriminated from normal infrared absorption bands by using the MAIRS technique.

1. Introduction

It is no exaggeration to say that the development of humankind depends on the function of available materials. In the 20th century, various chemistry disciplines have developed and it became possible to rationally create substances. This trend continues to this day, with major contributions from organic,[1),2)] inorganic,[3),4)] and polymer chemistry,[5),6)] which create molecules, and supramolecular chemistry,[7),8)] coordination chemistry,[9),10)] and material chemistry,[11),12)] which can combine these molecules in various ways. At the same time, basic physics[13),14)] and analytical science,[15),16)] which master the phenomena of matter, have unraveled the partial arrangement of newly created materials. Applied physics has also made a significant contribution in practical applications.[17)–20)] As these various scientific fields developed, scientists realized a common fact. That is, it is not the substance itself, but its structure and internal structure that have an extremely large impact on physical properties. In other words, it is important to control structure and develop functionality at the atomic, molecular, and nano-level for further advanced functions.

It was the inception and development of nanotechnology that determined this trend. Various scientific technologies that advocate nanotechnology make it possible to directly observe the structure of atoms and molecules.[21),22)] The physical properties of materials at the microscopic level are now being revealed.[23),24)] Various sensors,[25),26)] devices,[27),28)] energy-related functional systems,[29),30)] and biomedical materials[31),32)] have been developed, and many of them have nanostructures that enhance their functions. The elements of nanotechnology have been utilized in the development of materials. Just as the inception of nanotechnology has advanced physics and chemistry at the nanoscopic level, the establishment of some new concept is expected to dramatically aid this trend of development. An emerging concept of nanoarchitectonics plays this role.[33),34)] Just as Richard Feynman initiated nanotechnology in the mid-20th century,[35),36)] nanoarchitectonics was proposed by Masakazu Aono at the turn of the 21st century.[37)] Nanoarchitectonics is a concept that is positioned as post-nanotechnology.[38)]

Nanoarchitectonics integrates nanotechnology with various other research fields related to materials science. It uses nano-level knowledge to fabricate functional materials. It is the architecture of functional material systems by uniting atoms, molecules, and nanomaterials. It can be called material architecture science starting from nano. It is a

strategy that uses and combines physical and chemical material conversion, atomic and molecular manipulation, self-assembly and self-organization, orientation and organization by external forces and fields, fabrication at the nano and micro level, and biochemical processes to create functional materials from nanomaterials.[39),40)] These principles are not limited to specific materials and can be applied to many objects and applications. From the basics such as material synthesis,[41),42)] structure fabrication,[43),44)] physical phenomena,[45),46)] and biochemistry,[47),48)] nanoarchitectonics is used in catalysts,[49),50)] sensors,[51),52)] devices,[53),54)] and energy-related,[55),56)] environmental,[57),58)] and bio-related applications[59),60)] as more applied fields. Since all matter is originally made of atoms and molecules, the methodology of architecting functional material systems from atoms and molecules may be applied to all matter. In analogy to the ultimate theory in physics, the theory of everything,[61)] nanoarchitectonics may be said to be the method for everything in materials science.[62),63)]

Even though the methodology is applicable to all materials, there are some material forms that are favorable for application. One of the most promising forms is ultrathin films.[64),65)] Ultrathin films have a nano-level thickness but a practical-level lateral sizes. Therefore, nano-oriented phenomena can be reflected in a material of a practical size. If such a thin film is immobilized on a sensor or device, the nanophenomena that occur in response to external stimuli can be transmitted to the device. For example, when considering organic molecules as nano-units, self-assembled monolayer (SAM),[66),67)] Langmuir-Blodgett (LB) method,[68),69)] layer-by-layer (LbL) assembly,[70),71)] and other methods are used to create nanofilms. Ultra-thin films of organic semiconductors and other materials are also thin film forms with rich applicability.[72),73)] Especially, usages of functional thin films in applied physics fields are significant.

In addition to the fabrication of functional thin films, the development of analytical techniques is essential for the nanoarchitectonics of thin films and their applications in applied physics. These include techniques such as probe microscopy for direct observation of atomic and molecular images,[74),75)] and spectroscopic techniques such as photoelectron characterization.[76),77)] Vibrational spectroscopy, such as IR, is a versatile and very useful method for analyzing thin films of more general applicability.[78),79)] By looking at the vibrational spectra of bonds that are present in all molecules, one can evaluate the orientation of the molecule and the interactions between molecules in relation to specific functional

groups. In particular, the MAIRS (Multiple-Angle Incidence Resolution Spectrometry) method developed by Hasegawa et al. is a very powerful technique for analyzing the molecular orientation of organic thin film molecular assembly structures.[80)–82)] The MAIRS method is an analytical technique in which a sample is irradiated with polarized infrared light and the angle of incidence on the sample and the angle of polarization are changed while measuring. By obtaining the in-plane and out-of-plane vibration spectra of the thin film, not only the molecular orientation, but also the anisotropic characters of the film of the film can be analyzed. We would like to argue in this paper that this method is a very promising methodology to promote nanoarchitectonics research of thin films. The descriptions and discussions presented here demonstrate the potential of the MAIRS method to make a significant contribution to the development of functional material systems and their analysis for applications in applied physics.

For this purpose, this review describes the MAIRS method from its basics to the latest various developments. It actually covers analyses of molecular orientation and chemical reaction in thin films of organic semiconductors and polymeric films, as well as science of astronomy, sensor device analysis on nano-wires of ZnO in addition to phonon analysis targeted for fluorocarbons.

2. Fundamental background of MAIRS

2.1 Spectroscopic analysis of molecular orientation in thin films

Fundamentals of molecular orientation analysis in thin films by absorption spectroscopy are given by measurements of both parallel and perpendicular components of each transition moment, which can be correlated with the orientation angle defined from the surface normal.

When the analyte is a ‘thin film’ having the thickness, d, being much less than the wavelength, λ, of the probe light ($d/\lambda \ll 1$), the surface–parallel (in-plane; IP) and –perpendicular (out-of-plane; OP) absorptions denoted as A_{IP} and A_{OP}, respectively, are observed as:[83),84)]

$$A_{\mathrm{IP}} \propto \mathrm{Im}\left(\varepsilon_{\mathrm{r},x}\right) = 2nk_x \tag{1}$$

$$A_{\mathrm{OP}} \propto \mathrm{Im}\left(-\frac{1}{\varepsilon_{\mathrm{r},z}}\right) \approx 2\eta nk_z \qquad (\text{if } n^2 \gg k_z^2). \tag{2}$$

Here, ε_{r} is electric relative permittivity, and *x* and *z* show the surface–parallel and –perpendicular directions, respectively. In addition, *n* and *k* are the real and imaginary parts of complex refractive index, $\tilde{n}$ ($\equiv n+\mathrm{i}k=\sqrt{\varepsilon_{\mathrm{r}}}$), respectively, and *n* is approximated to be common to both IP and OP spectra. The functions of $\mathrm{Im}\left(\varepsilon_{\mathrm{r},x}\right)$ and $\mathrm{Im}\left(-1/\varepsilon_{\mathrm{r},z}\right)$ are known as the transverse-optic (TO) and longitudinal-optic (LO) energy-loss functions, respectively. The proportionality in the equations reflects Fermi's golden rule, and η is a proportional coefficient that is for the sensitivity ratio between A_{IP} and A_{OP}.

If the molecules in the thin film are uniaxially orientated ($k_x = k_y$), the following equation holds.[85)]

$$k_{\mathrm{ave}} \equiv \frac{k_x + k_y + k_z}{3} = \frac{2k_x + k_z}{3} \tag{3}$$

Here, k_{ave} is the averaged (orientation free) extinction coefficient. If extremely oriented cases are considered, the following two equations are thus obtained.

$$\text{Surface parallel } (k_z = 0):\ k_{\mathrm{ave}} = \frac{2k_x}{3} \ \Leftrightarrow\ k_x = \frac{3}{2}k_{\mathrm{ave}} \tag{4}$$

$$\text{Surface perpendicular } (k_x = 0):\ k_{\mathrm{ave}} = \frac{k_z}{3} \ \Leftrightarrow\ k_z = 3k_{\mathrm{ave}} \tag{5}$$

When the orientation angle, ϕ, is considered, the two equations are thus respectively modified to have the ellipsoid of the extinction coefficient:[85)]

$$k_x(\phi) = \frac{3}{2}k_{\mathrm{ave}}\sin^2\phi \tag{6}$$

$$k_z(\phi) = 3k_{\mathrm{ave}}\cos^2\phi \tag{7}$$

Combining Eqs (1), (2), (6) and (7) gives Eq (8).

$$\phi = \tan^{-1}\sqrt{\frac{2\eta A_{\mathrm{IP}}}{A_{\mathrm{OP}}}} \tag{8}$$

Conventionally, A_{IP} and A_{OP} are measured absorbance at a wavenumber by the transmission (Tr) and reflection-absorption (RA) spectrometries,[83),84)] respectively, which means that the two different techniques are necessary. Since the two technique needs different substrates for supporting thin films, i.e., infrared transparent and mand co-

workerslic substrates, we very often encounter a problem that an identical film cannot be prepared on the two different substrates. In addition, the difference of sensitivity of RA from Tr ($\eta \neq 1$) is another big problem for quantitative analysis of molecular orientation because it requires highly complicated electrodynamic calculations to obtain η using optical parameters for every absorption peak.[85] To overcome the intrinsic and long-term unsolved issue, another totally different idea is necessary. MAIRS[80)–82)] is built for solving this problem, which is described in the next section.

2.2 Birth of MAIRS

Most of the spectroscopic techniques are exactly based on physical theories that are deduced from fundamental physical principles, which makes us possible to quantitatively analyze the samples with high precision. At the same time, however, this orthodox approach makes a limit that every measurement technique has different sensitivity from the others.

To get over the limitation on a common sense of theoretical physics, a largely different mathematical framework is introduced i.e., regression equation.[83)] The term of 'regression' is used as the meaning of 'prediction,' and the most fundamental one is the classical least squares (CLS) regression. CLS regression makes the measured absorbance spectra, $\boldsymbol{A}$, modeled by the pure constituent spectra, $\boldsymbol{K}$, using the concentration matrix, $\boldsymbol{C}$.

$$\boldsymbol{A} = \boldsymbol{C}\boldsymbol{K} + \boldsymbol{U} \tag{9}$$

Here, $\boldsymbol{U}$ is the matrix receiving unmodeled factors and experimental errors.[83)]

CLS regression is known to work out with a very good analytical accuracy if the number of constituents involved in the system is surely available with their concentrations. In other words, if unexpected chemical components appear in the system making the concentration information uncertain, the analytical accuracy runs down severely.[83)] In general, the chemical constituents are of all the components including unexpected ones such as molecular associates and solvated molecules, which makes the number of constituents different from the information known in advance. Therefore, the CLS technique is not employed for practical chemical analysis often.

However, if the constituents were of "polarization of light" for thin film analysis, the situation changes greatly. Since the electric field of light that determines the direction of linear polarization can only be parallel and perpendicular to the film surface, the constituents of polarizations are exactly fixed at two, and they cannot be three or more.

In addition, another important idea is necessary: light 'intensity' spectra, $\boldsymbol{S}$, must be applied to the CLS technique. If the 'absorbance' spectra are subjected to the CLS modeling, optical parameters are necessary because the sample and background spectra are treated at once in this process. As a result, the new technique is described as follows.

$$\boldsymbol{S} = \boldsymbol{R}\begin{pmatrix} \boldsymbol{s}_{\mathrm{IP}} \\ \boldsymbol{s}_{\mathrm{OP}} \end{pmatrix} + \boldsymbol{U} \tag{10}$$

Here, $\boldsymbol{R}$ stores the ratio factors for the linear combination of $\boldsymbol{s}_{\mathrm{IP}}$ and $\boldsymbol{s}_{\mathrm{OP}}$. The deduction process of the matrix elements in $\boldsymbol{R}$ (Eq. (11)) that is a function of the angles of incidence, θ, is a little bit complicated, and the reader is thus referred to refence.[80)]

$$\boldsymbol{R} = \begin{pmatrix} 1+\cos^2\theta+\sin^2\theta\tan^2\theta & \tan^2\theta \\ \vdots & \vdots \end{pmatrix} \tag{11}$$

Once $\boldsymbol{R}$ at several angles of incidence and the measured $\boldsymbol{S}$ are both ready, $\boldsymbol{s}_{\mathrm{IP}}$ and $\boldsymbol{s}_{\mathrm{OP}}$ are readily calculated as the least-squares solutions.[83)]

$$\begin{pmatrix} \boldsymbol{s}_{\mathrm{IP}} \\ \boldsymbol{s}_{\mathrm{OP}} \end{pmatrix} = \left(\boldsymbol{R}^{\mathrm{T}}\boldsymbol{R}\right)^{-1}\boldsymbol{R}^{\mathrm{T}}\boldsymbol{S} \tag{12}$$

The superscript, T, on the right shoulder of $\boldsymbol{R}$ indicates the transpose matrix. This analysis is repeated twice for the sample (film on substrate) and background (BG; substrate only) to have two sets of $\boldsymbol{s}_{\mathrm{IP}}$ and $\boldsymbol{s}_{\mathrm{OP}}$, and they are used to have the final results of $\boldsymbol{A}_{\mathrm{IP}}$ and $\boldsymbol{A}_{\mathrm{OP}}$ in the following manner.

$$\boldsymbol{A}_{\mathrm{IP}} = -\log_{10}\frac{\boldsymbol{s}_{\mathrm{IP}}^{\mathrm{sample}}}{\boldsymbol{s}_{\mathrm{IP}}^{\mathrm{BG}}} \quad \text{and} \quad \boldsymbol{A}_{\mathrm{OP}} = -\log_{10}\frac{\boldsymbol{s}_{\mathrm{OP}}^{\mathrm{sample}}}{\boldsymbol{s}_{\mathrm{OP}}^{\mathrm{BG}}} \tag{13}$$

Here, the division of the two vectors are performed at every scalar value in order.

The angles of incidence are critically important to make $\boldsymbol{A}_{\mathrm{IP}}$ and $\boldsymbol{A}_{\mathrm{OP}}$ have the common ordinate scale. This optimization of the angles has already been determined by using a calibration sample, and the calibration details are described in a reference.[86)]

2.3 pMAIRS

For quantitative analysis, another problem is figured out: the sensitivity of spectrometer for $\boldsymbol{s}_{\mathrm{IP}}$ is different from that for $\boldsymbol{s}_{\mathrm{OP}}$ at every wavelength. Since this polarization dependence of spectrometer can be measured by single-beam spectra of linear

polarizations at 0º and 90º, the correction function can be obtained that should work for reducing the polarization dependence theoretically. To our experiences, however, such kind of experimental correction does not work perfectly, and analytical inaccuracy remains. To overcome this problem, the s-polarization is excluded, and only the p-polarization is employed for the MAIRS measurements. This is named pMAIRS.[81)]

To remove the s-polarization contribution from the original MAIRS, the MAIRS matrix, $\boldsymbol{R}$, is a little bit modified for obtaining the pMAIRS matrix, $\boldsymbol{R}_{\mathrm{p}}$.

$$\boldsymbol{R}_{\mathrm{p}} = \begin{pmatrix} \cos^2\theta + \sin^2\theta \tan^2\theta & \tan^2\theta \\ \vdots & \vdots \end{pmatrix} \tag{14}$$

The rest processes of the MAIRS analysis need not to be changed for operating pMAIRS. The angles for pMAIRS optimized for representative substrates are presented in Table 1. The angles of incidence optimized must strictly be kept unchanged. As long as these angles are employed, η in Eq is unity.[81)]

Table 1 Experimental parameters for pMAIRS

Substrate	n_{sub}	Angles of incidence / º	Angle interval / º	H
Ge	4.0	9 – 44	5	0.15
Si	3.4	9 – 44	5	0.14
ZnSe	2.4	9 – 44	5	0.13
CaF_2	1.4	8 – 38	6	0.21

Here, n_{sub} is refractive index of the substrate. The angles of incidence show the range of angle with the angle interval. For example, when a germanium substrate is employed, the single-beam measurements are performed from 0º through 44º by 5º steps, and eight spectra are collected.

The parameter of H in the last column is necessary especially for substrates having a relatively low refractive index such as ZnSe and CaF_2. Details are described elsewhere,[87)] but we have to say accurate analysis requires Eq. (15) where n is the refractive index of the analyte thin film.

$$\phi = \tan^{-1}\sqrt{\frac{2A_{\mathrm{IP}}}{n^4 H A_{\mathrm{OP}}}} \tag{15}$$

The parameter of H is automatically set on actual commercial spectrometers. What we have to do is only selecting the substrate, and we don't have to be concerned about H and and angles as well. Refractive index of the thin film of organic compounds can typically be set

to 1.55. If the film is of fullerene and perfluoroalkyl compounds having unusual index, however, they should be set to 1.80 and 1.35 respectively. If detailed value of the index is available, it should be used for the orientation angle analysis.

One of the benefits of using pMAIRS is that the analytical accuracy of the orientation angle is quite high, which attains the three significant figures if the film surface is highly flat as found in Langmuir-Blodgett films, evaporated films, and self-assembled monolayers. Figure 1 presents IR pMAIRS spectra of pentacene evaporated on a silicone substrate. As is always found in MAIRS, pMAIRS provides two spectra of the IP and OP ones simultaneously from an identical thin film sample.

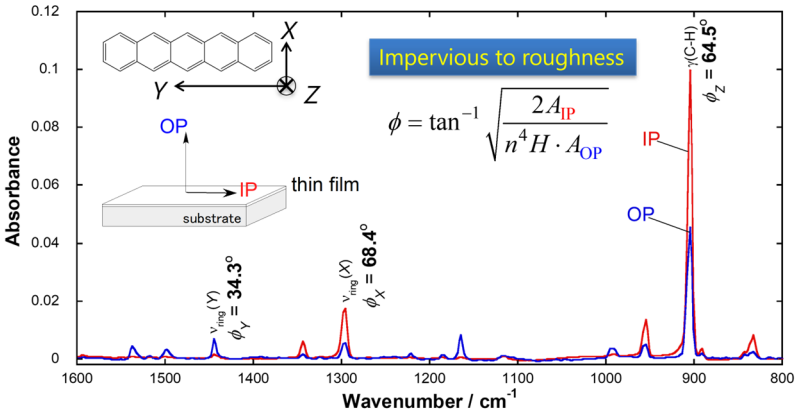

Figure 1. IR pMAIRS spectra of pentacene film evaporated on silicon. The red and blue curves are the IP and OP spectra, respectively.[82)]

Since the spectra are optimized to have a common ordinate scale, the orientation angle can readily be calculated by using Eq. (15) with H in Table 1. The calculated angles for the transition moments along the x, y, and z axis of the molecule are shown in the figure. The three axes are mutually orthogonal because of the stiffness of pentacene, and therefore the three angles should satisfy the direction cosine equation (Eq. (16)).

$$\cos^2\phi_x + \cos^2\phi_y + \cos^2\phi_z = 1 \qquad (16)$$

If the three analyzed angles are put in this equation, the summation is calculated to be 1.00 as predicted theoretically. This agreement straightforwardly indicates that pMAIRS performed with Table 1 works very good with an analytical accuracy of three significant figures.

In addition, the analytical accuracy relatively keeps well even for thin films having surface unevenness. This is because the unevenness influences nearly equally to both IP and

OP spectra, and the influences are cancelled by making the ratio of $\boldsymbol{A}_{\mathrm{IP}}$ and $\boldsymbol{A}_{\mathrm{OP}}$ in Eq. (15). This property of MAIRS is powerful and unique as a spectroscopic technique. Thanks to this characteristic, practically useful thin films such as spin-coated films and drop-casted films can be analyzed quantitatively. To our experiences, as long as the RMS value of atomic-force microscopic (AFM) analysis is less than 100 nm, the analytical accuracy is less than 10%.

2.4 MAIRS2

Basically, pMAIRS works well with most thin films, but we sometimes encounter practical problems. The first one is imperfect subtraction of water-vapor peaks mostly in the finger-print region after the measurements. The second one is that optical fringes appear in the spectra. These problems are not found only for pMAIRS specifically, and they appear even in normal-incidence transmission spectra. In fact, these are common annoying problems often found in IR spectra measurements, and they have long been believed to be difficult issues that cannot be overcome.

Shioya and co-workers found that these problems became stronger when the substrate had a larger refractive index.[88] If the light is incident at the air/substrate interface perpendicularly from the air phase, the reflectance, R, is given by:

$$R = \left(\frac{n_{\mathrm{substrate}} - 1}{n_{\mathrm{substrate}} + 1} \right)^2 . \qquad (17)$$

Since this is an increasing function with the refractive index of the substrate ($n_{\mathrm{substrate}} > 1$), a larger index gives a larger reflectance. This means that a substrate with a large index makes a portion of the incidental IR light go back to the interferometer in FT-IR and ‘double modulation’ happens there. Since FT-IR does not take such an extraordinary modulation into account, this makes the results distorted making the subtraction of water-vapor peaks imperfect.

To prevent the going-back of the reflected light to the interferometer, small angles of incidence should not be employed. On this concept, a new technique employes the angle of incidence fixed at 45°, and instead the polarization of the incidental light is changed to carry out the MAIRS measurements. This 2nd generation technique of MAIRS is named MAIRS2. The new technique not using a low angle of incidence also makes the matter of optical fringes improved greatly because the fringes are enhanced at a low angle of incidence.

Figure 2 presents IR MAIRS2 spectra as well as pMAIRS spectra of spin-coated film of poly(2-perfluorobutyletyl acrylate) deposited on a silicon substrate. In the pMAIRS spectra, water-vapor peaks and optical fringes are found both removed effectively. This makes minor peaks visible and the peak positions highly accurate.

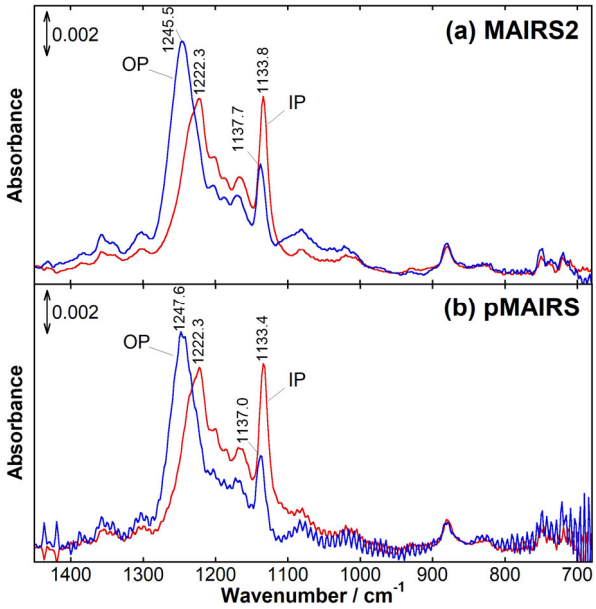

Figure 2. IR spectra of poly(2-perfluorobutyletyl acrylate) spin-coated film on Si measured by (a) MAIRS2 and (b) pMAIRS techniques. The red and blue curves are the IP and OP spectra, respectively.

3. Practical Applications of MAIRS

3.1 Organic semiconductor analysis in thin films

Organic semiconductors have a condensed ring structure consisting of π-conjugated systems, and the orientation of the aromatic rings determines the direction of charge transport in thin films. Therefore, accurate understanding and control of molecular orientation is extremely important for the development of high-performance thin-film devices.[89)–92)] Molecular orientation of organic semiconductors can roughly be classified into two types with respect to the aromatic rings to the substrate: the end-on and edge-on orientations. The edge-on orientation can further be divided into two types depending on the orientation of the long axis of the molecule, but for the sake of simplicity, we will refer to both types of orientation as edge-on orientation.

Since face-on and edge-on orientations show contrasting aptitudes for the devices in which they are used, it is important to develop analytical methods to identify the molecular

orientation in thin films. For this purpose, the MAIRS technique is powerful because it can directly discuss the orientation of aromatic rings. In fact, this method has been used for molecular orientation analysis of many thin-film organic semiconductor materials,[93)–116)] such as poly(3-alkylthiophene)s,[93)–98)] polyphyrins,[99)–104)] and pentacene (PEN).[105)–109)]

To analyze the molecular orientation of organic semiconductors, the C–H out-of-plane vibrational (γ(CH)) band of aromatic rings is useful because of its high absorption intensity and its direction of the transition moment. An additional advantage of using the γ(CH) band for orientation analysis is that it does not overlap with other vibrational bands because it appears in the wavenumber region below 950 cm^{-1}, which is outside the fingerprint region. In fact, by focusing on the intensity of the γ(CH) band in the pMAIRS spectra, the face-on and edge-on orientations of organic semiconductors can easily be distinguished.[93),94),96)–103),105)–111)] We will introduce some examples of studies in which the pMAIRS technique is used to analyze the molecular orientation of organic semiconductors on solid substrates as follows.

PEN is one of the most well-studied organic thin-film semiconductor materials, and much interest is focused on its aggregation structure in the film in terms of molecular orientation as well as the polymorphs. When this compound is stacked on a solid substrate, the edge-on orientation is typically formed due to its high self-assembling property.[117)–119)] On the other hand, there are reports that exceptionally non-oriented thin film structures can be obtained by making the substrate temperature (T_{sub}) low during the deposition process,[120)–124)] but the details of the structure have long been unknown.

The pMAIRS technique is useful for analyzing the molecular orientation of such low-crystalline thin films. The molecular orientation of PEN in thin films fabricated at room temperature (T_{sub} = 298 K) and at low temperature (T_{sub} = 210 K) is revealed by using pMAIRS spectra.[105)] When the γ(CH) bands that typically appear at about 905 cm^{-1} in these films are compared, the IP and OP band intensity ratios are found inverted (Figure 3a). This result clearly indicates that they have totally different molecular orientations from each other. Since the γ(CH) mode of the aromatic ring has a transition moment perpendicular to the ring plane, the observed MAIRS dichroism indicates that the PEN molecules have an edge-on orientation in the room temperature deposition film while a face-on orientation in the low temperature-deposited film. In other words, by using the pMAIRS spectra, the unusual

molecular orientation of PEN in the low-temperature evaporated film on Si was revealed for the first time.

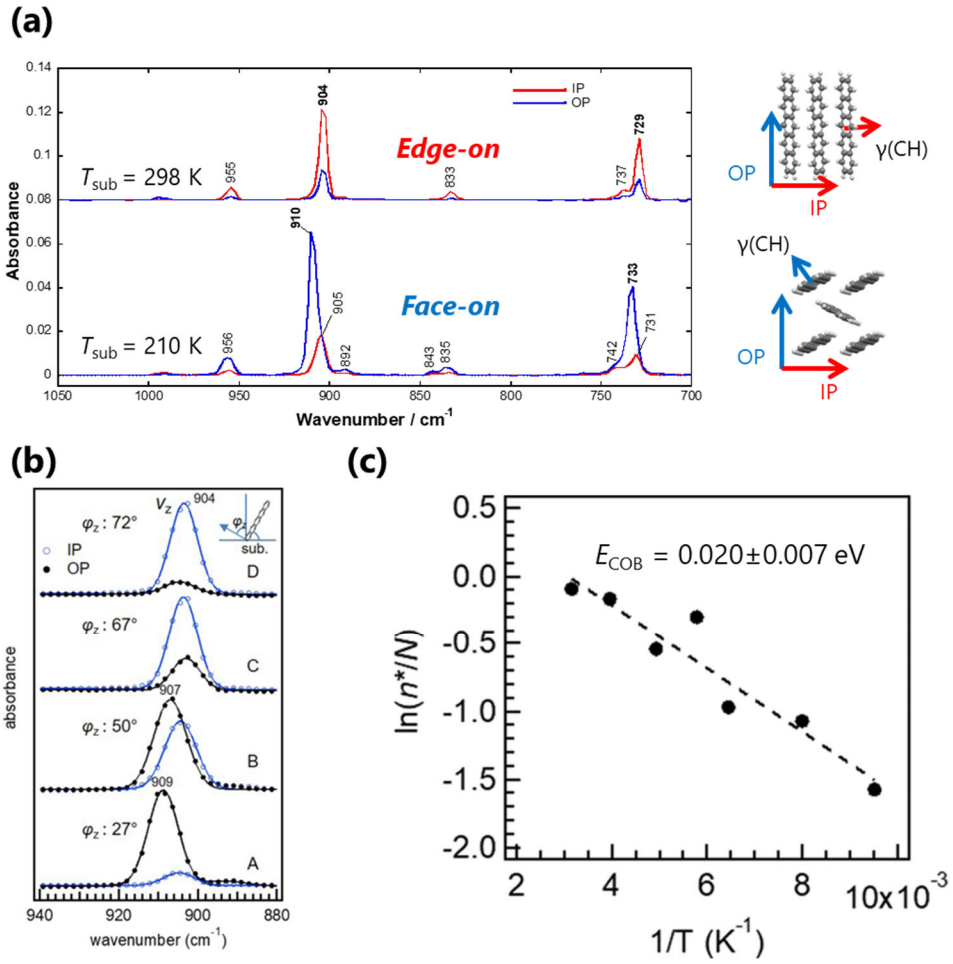

Figure 3 (a) IR-pMAIRS spectra of pentacene thin films prepared at 298 K and 210 K. (b) pMAIRS spectra for pentacene films in the wavenumber position of 940-880 cm^{-1}.[105] [DOI: 10.1038/s41598-018-37166-6] (b) pMAIRS spectra for pentacene films in the wavenumber position of 940–880 cm^{-1} where IP (blue open circle) and OP (black filled circle) spectra are plotted with fitted curves (IP: blue solid line, OP: black solid line). Inset shows a schematic illustration of the orientation angle ϕ_z of peak ν_z are denoted for each spectrum. Inset shows a schematic illustration of the orientation angle, ϕ, of a pentacene molecule against a substrate (sub.). (c) Logarithm of the component ratio of standing molecules to all molecules $\ln(n^*/N)$ vs inverse temperature ($1/T$). Dotted line represents a least-squares fit. The correlation coefficient is 0.90.[108] The correlation coefficient is 0.90. [DOI: 10.1103/physrevmaterials.5.013801].

Nagai and co-workers estimated the existence ratio of the edge-on and face-on orientations in thin films from the pMAIRS dichroism that is used for determination of the activation energy by plotting the Arrhenius plot in Figure 3b and c) [108),109)]. This was further

induced to be a collective orientation change (E_{COB}: collective orientation barrier). E_{COB} can be used as an indicator of the likelihood of collective orientation change. In fact, the E_{COB} of PEN thin films on silicon oxide (SiO_2) and graphene are 0.02 eV and 0.20 eV, respectively, indicating that molecules on graphene are less likely to form edge-on orientations. This result quantitatively shows that the graphene surface interacts with the π-conjugated surface of PEN to suppress the edge-on orientation of molecules, and thus acts as a template layer.[125] The results quantitatively show that the graphene surface interacts with the π-conjugated surface of PEN, thereby inhibiting rising up of the molecules. The pMAIRS technique can conveniently be used for quantitatively discussing the orientation properties of semiconductor molecules on a particular substrate of interest.

Another example of molecular orientation analysis is presented for zinc tetraphenylporphyrin (ZnTPP) in amorphous films.[101] ZnTPP has a chemical structure consisting of a porphyrin ring and four phenyl groups.[99] Grazing incidence X-ray diffraction (GIXD) patterns of evaporated films of this compound at room temperature show that the molecules form an amorphous structure, independent of the evaporation rate (Figure 4a). The GIXD result gives the prediction that the ZnTPP molecules are unoriented in the deposited film. The analysis based on the pMAIRS spectra, however, overturns this prediction. Focusing on the γ(CH) band of porphyrin at 798 cm^{-1} in Figure 4b, a strong OP band is clearly observed when the film is deposited at a relatively high deposition rate (80 nm min^{-1}). On the other hand, thin films deposited at a lower deposition rate (0.2 nm min^{-1}) have almost the same intensity of the IP and OP bands. This suggests that the high deposition rate results in formation of a kinetically controlled face-on orientation. In this manner, the combination technique of GIXD and pMAIRS makes it possible to discuss both crystallinity

and orientation in thin films individually, which means that pMAIRS serves as a complementary technique to GIXD.

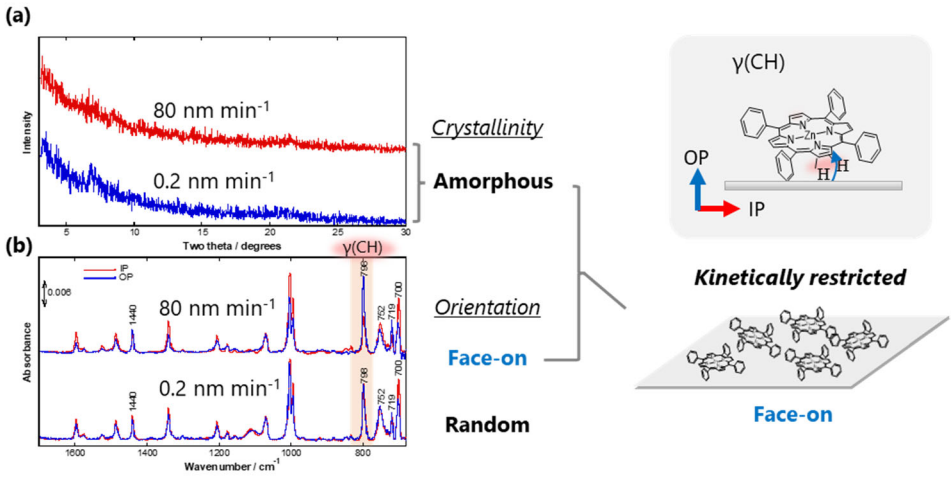

Figure 4 (a) GIXD patterns and (b) pMAIRS spectra of fast and slow-deposited films of ZnTPP prepared at ambient temperature.[101] [DOI: 10.1021/acs.jpcc.8b00972].

Another advantage of using the pMAIRS technique is that the structure can be discussed for each functional chemical group. This feature is particularly important for the structural analysis of organic semiconductor materials having alkyl side chains such as 2-decyl-7-phenyl[1]benzothieno[3,*2*-*b*][1]benzothiophene (Ph-BTBT-C_{10}).[126] Figure 5a, this compound has different polymorphs of crystal and liquid crystal in thin films depending on temperature: thin film phase,[127] bulk phase,[128] and smectic E (SmE) phase.[129] While the polymorphism of Ph-BTBT-C_{10} in thin films has already been elucidated in this manner, the structure of the alkyl chains in the crystal structure is not yet understood. In particular, it should be noted that the crystal structures of the thin film and SmE phases were obtained based on X-ray diffraction (XRD) patterns, assuming that the alkyl chains have the all-trans-zigzag conformation.[127),129] In other words, the structure of the alkyl side chain cannot be determined by the XRD patterns alone. In such cases, structural analysis using pMAIRS

works powerfully to determine the conformation of the alkyl side chains and the orientation as well.

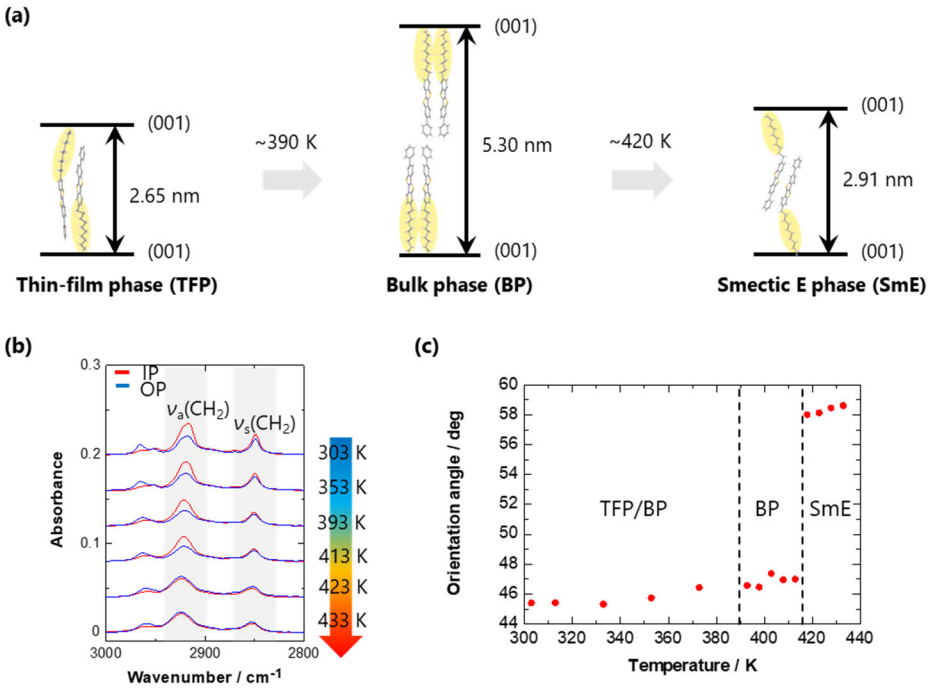

Figure 5 (a) Crystalline polymorphs of Ph-BTBT-C10 : bulk phase (BP), thin-film phase (TFP), and smectic E phase (SmE). (b) IR pMAIRS spectra of thin films measured at several temperatures and (c) average orientation angles of the decyl chain calculated from the pMAIRS spectra.[115] [DOI: 10.1021/acs.jpclett.2c03399].

The CH_2 symmetric and antisymmetric stretching vibration bands ($\nu_s(CH_2)$ and $\nu_a(CH_2)$, respectively) are typically used to discuss the structure of alkyl chains.[130)–132)] Indeed, the structure of the decyl group of Ph-BTBT-C_{10} has been analyzed on the basis of the temperature dependence of these vibrational bands.[115)] Looking at the pMAIRS spectrum of the as-deposited film (303 K), both $\nu_s(CH_2)$ and $\nu_a(CH_2)$ bands appear strongly in the IP spectrum (Figure 5b). This indicates that the alkyl chains are oriented upright, which is typical for the formation of aggregate structures. At the same time, the wavenumber positions of the bands indicate that the decyl chains have the all-trans-zigzag conformation. In other

words, considering that Ph-BTBT-C_{10} is actually in the thin film phase in this temperature range, and the model structure of the decyl group in the thin film phase shown in Figure 5a is supposed to be true. On the other hand, above the transition point to the SmE phase (~420 K), the IP and OP spectra are almost identical to each other (Figure 5b and c), which clearly indicates that the orientation of the decyl chains has changed to be a disordered state due to melting. This result is consistent with the fact that the SmE phase can be regarded as a crystalline phase in crystallographic terms.[133] This provides important evidence that this phase is essentially a liquid crystalline phase. Thus, the pMAIRS technique is useful for elucidating the orientation of the side chains as well as the π-conjugated backbone.

3.2 Quantitative analysis of on-surface reactions

In the above, we have shown that the pMAIRS technique has a characteristic that IP and OP spectra are obtained on a common vertical axis scale, which enables us to quantitatively analyze molecular orientation in thin films. This unique property of the pMAIRS technique provides another advantage of giving optically isotropic (OI) spectra by averaging the IP and OP spectra (Eq. 1).[106]

$$A_{\mathrm{iso}} = \frac{1}{3}\left(2A_{\mathrm{IP}} + A_{\mathrm{OP}}\right) \tag{18}$$

Here, A_{iso}, A_{IP} and A_{OP} denote the absorbance of the OI, IP, and OP spectra, respectively. In other words, by substituting the measured IP and OP spectral intensities into Eq. (18), the spectra of the unoriented molecules can be obtained by the simple calculation. Since the OI spectrum is independent of molecular orientation, the band intensity in the OI spectrum is solely proportional to the quantity of chemical species in the thin film. Therefore, from the intensity of the OI spectrum, the quantitative changes of chemical species associated with chemical reactions can be analyzed in the thin film (often called on-surface

reactions).[106),134)–136)] This further makes it possible to estimate thermodynamic constants such as rate constants and activation energies.[135)] In the following, we will introduce examples of studies in which the pMAIRS technique is applied to the analysis of on-surface reactions.

13,6-N-sulfinylacetamidopentacene (SAP), one of the typical precursor materials of PEN, is readily converted to the desired product by heat treatments.[137)] The overall picture of this on-surface reaction is investigated by multivariate analysis of pMAIRS spectra measured at several annealing temperatures.[106)] The results reveal that the compounds appeared in the reaction are of three chemical species and the ratios of these components can be quantitatively revealed (Figure 6). The conversion reaction of SAP to PEN is initiated at an annealing temperature of about 400 K, and is almost completely completed by 420 K. In this stage, PEN is produced in the two forms of the "thin film" and "bulk" phases simultaneously. As the temperature increases, the thin-film phase is converted to the bulk phase, and the thin-film phase is mostly annihilated eventually.

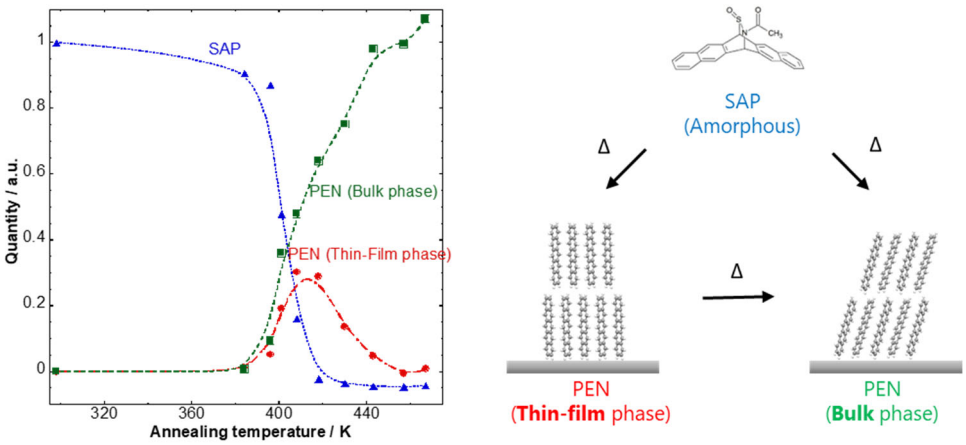

Figure 6 Quantity variations of the three chemical constituents in the SAP/PEN mixed thin films as a function of thermal treatment temperature analyzed by classical least-squares regression calculation. Quantity variations of the three chemical constituents in the SAP/PEN mixed thin films as a function of thermal treatment temperature analyzed by classical least-squares regression calculation.[106)] [DOI 10.1021/acs.jpca.0c00111].

The thermal conversion of dinaphtho[2,3-b:2′,3′-f]thieno[3,2-b]thiophene (DNTT) precursors has also been analyzed using a similar approach.[134] DNTT-phenylmaleimide monoadduct, one of the DNTT precursors, has several stereoisomers, among which endo (5,14-)[138] and exo (5,14-) forms[139] are commercially available as precursor materials for organic thin-film transistors. Nevertheless, the exo isomer shows almost no conversion reaction to DNTT in spin-coated thin films, as revealed for the first time by analysis using the pMAIRS technique (Figure 7). On the other hand, the reaction of endo isomers proceeded quantitatively. The difference in stereoisomer-dependent reactivity was also found to be due to the molecular aggregation structure of the precursor, as shown schematically in Figure 7.

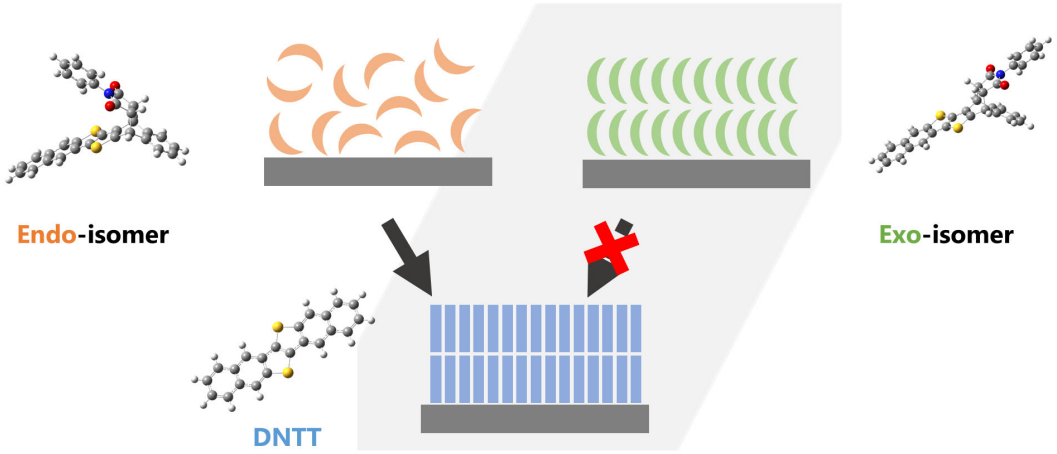

Figure 7 Structural conversion reaction of DNTT precursors.

Recently, Maruyama and co-workers developed an in-situ measurement system combining an FT-IR system involving MAIRS2 and a vacuum deposition system to investigate the formation process of organic and inorganic halide perovskite thin films (Figure 8a).[135] To incorporate the MAIRS technology into a vacuum chamber, MAIRS2 is fairly suitable because the angle of incidence is fixed in MAIRS2. In this study, $C(NH_2)_3I$

(guanidine hydroiodide: GAI) and SnI_2 were used as organic and inorganic sources, respectively. GAI/SnI_2 bilayer thin films were prepared by vacuum evaporation using a continuous wave IR laser (CW-IR).[140),141)] The isothermal conversion reaction from the precursor film to the $GASnI_3$ perovskite film was pursued by the MAIRS2 technique. The reaction products were quantified from the obtained spectra, and the dependence of the $GASnI_3$ formation rate on the reaction temperature was analyzed using the Avrami model. As a result, this reaction was found to be a diffusion-controlled reaction. Furthermore, the activation energy of the reaction was estimated to be 67 ± 11 kJ mol^{-1} by means of an Arrhenius plot (Figure 8b). Thus, the MAIRS2 technique is useful not only for the analysis of molecular orientation in thin films, but also for elucidating the kinetics of on-surface reactions.

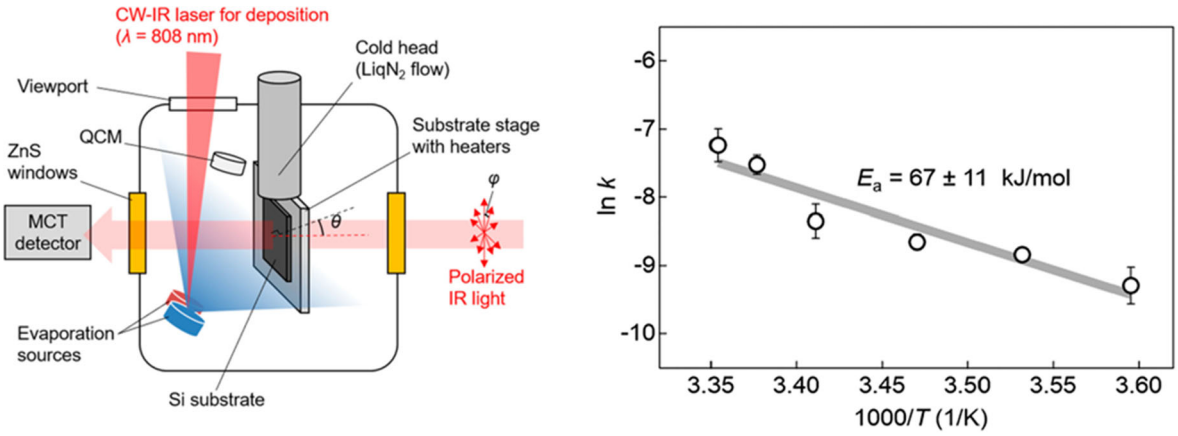

Figure 8 (a) A schematic illustration of the in-situ FT-IR/vacuum deposition system. (b) Arrhenius plot of the reaction rate constant (k) estimated from the Avrami model.[135)] [DOI: 10.1021/acsami.3c08708].

3.2 Protein analysis in Langmuir-Blodgett films

Langmuir-Blodgett (LB) films, which are formed at the air–water interface[142),143)], is a powerful platform providing insight into the molecular interactions of cell membranes, proteins, and other molecules.[144)] The MAIRS technique is useful for elucidating molecular

interactions in LB films, and it has been used to study the interactions of amphiphilic compounds[80),145)–149)], as well as peptides and proteins.[150)–152)] The molecular orientation and conformation at the air-water interface of peptides and proteins, as well as amphiphilic compounds, can quantitatively be discussed. As an example, Wang and co-workers employ the pMAIRS technique for analyzing the molecular orientation and conformation of α-synuclein[153)–156)] that is known to be deposited on cell membranes and causes Parkinson's disease.[157),158)] α-synuclein consists of 140 amino acids and the nonamyloid component (NAC), which corresponds to a sequence of 61-95 amino acids, is known to be responsible for the deposition of α-synuclein on the plasma membrane.[159)] C. Wang and co-workers synthesized α-synuclein (61-95) consisting only of NAC sites and LB films of the synthesized one were prepared.[157)] Circular Dichroism (CD) spectra of the LB films showed that the NAC moiety alone also forms an α-helix in the LB films as found for α-synuclein.[160)]

The pMAIRS spectra of the LB film were then used to estimate the tilt angle of the α-helix formed by the NAC moiety relative to the substrate. For this analysis, the amide I band at 1658 cm^{-1} derived from the α-helix was used (Figure 9).

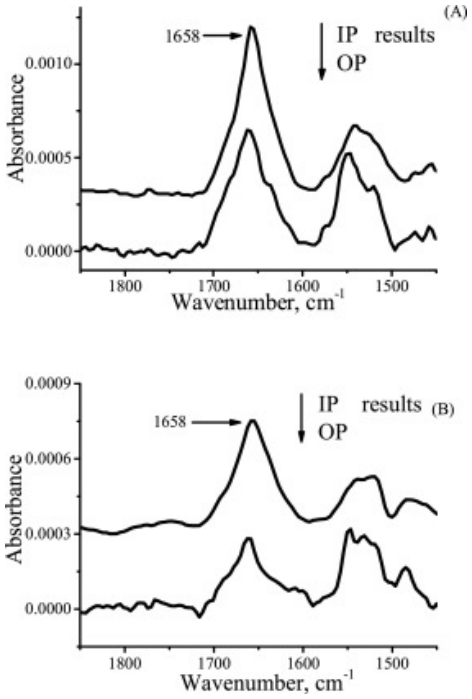

Figure 9 p-MAIRS results of the LB film of α-synuclein (61-95) transferred under 6 mN m^{-1} (A) and 10 mN m^{-1} (B).[157] https://doi.org/10.1016/j.colsurfb.2019.110401

The pMAIRS-IP and -OP spectra of the amide I band indicate that the helical axis of the α-helix is tilted approximately 30° from the substrate. However, macroscopic IR spectroscopy provides only average information for the entire thin film. Therefore, in addition to the NAC model in which the entire α-helix is tilted at 30° at the air-water interface, a bent chain model in which the hydrophilic part of the α-helix is oriented horizontally to the water surface while the hydrophobic part rises above the water surface is also possible (Figure 10).

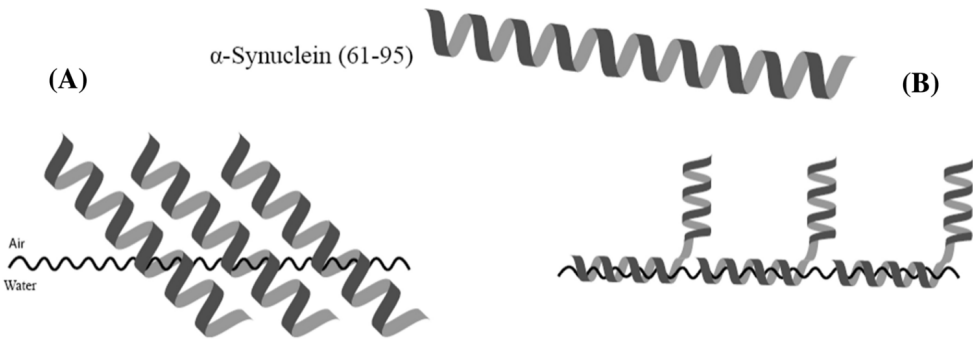

Figure 10 Illustration of two possibilities of α-synuclein (61-95) at the air–water interface.[158] https://doi.org/10.1007/s44211-022-00128-0

The orientation of the α-helix in the LB film was therefore discussed by introducing the carbon isotope ^{13}C into the 93rd glycine near the C-terminus of α-synuclein (61-95).[158] Therefore, the backbone carbonyl (C=O) group of glycine at the position 93 near the C-terminus of α-synuclein (61-95) was labeled with ^{13}C [161] and by comparing the amide I bands at ^{12}C and ^{13}C.[162] CD spectra of LB films showed that α-synuclein (61-95) labeled with ^{13}C also forms an α-helix. pMAIRS-IP spectra showed amide I and II bands at 1655 and 1535 cm^{-1}, which are derived from the α-helix (Figure 11). The band at 1625 cm^{-1} would be attributed to the amide I band involving ^{13}C. The CD spectrum shows no β-sheet peak, and since the band of α-helices with amide I involving ^{13}C is known to shift a low wavenumber by about 30~40 cm^{-1}, the band at 1625 cm^{-1} is also considered to be derived from the α-helix.[161] The pMAIRS-OP band is also known to be derived from the α-helix. On the other hand, in the pMAIRS-OP spectrum, the amide I band splits into 1659 and 1645 cm^{-1}. Furthermore, the amide I band labeled with ^{13}C at 1625 cm^{-1} is very weak in intensity. This indicates that the labeled amide I band is suggested to be oriented in-plane. Thus, by incorporating the labeled protein into an LB film. The pMAIRS spectrum of the LB film, we obtained a schematic that α-synuclein (61-95) forms an α-helix at the air-water interface with

an orientation such that the site near the C-terminus is horizontal and the opposite N-terminal site stands vertically.

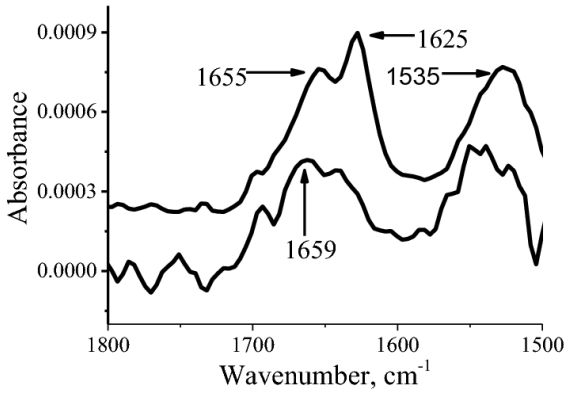

Figure 11 pMAIRS results of the LB monolayer of the ^{13}C labeled α-synuclein (61-95) at position 9 glycine prepared at 10 mN m^{-1} on silicon slide. The top curve is the the IP spectrum and the bottom one is OP spectrum.[158)] https://doi.org/10.1007/s44211-022-00128-0

3.3 Liquid crystalline polymers

In the analysis of thin films composed of soft materials such as polymers and liquid crystals, XRD is a primarily powerful method, but it can only provide information on crystalline portions. MAIRS can discuss the molecular conformation and orientation of specific functional groups, no matter how the crystallinity is in the thin film. Therefore, for polymer liquid crystal thin films with a mixture of crystalline and disordered regions, the combined technique of XRD and MAIRS works powerfully to analyze the crystallinity and orientation in an identical thin film.[163)–165)]

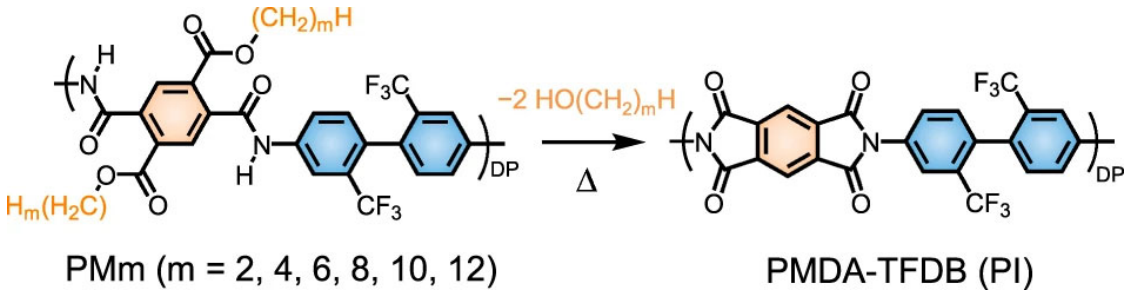

Figure 12 Chemical structures of the target poly(amic n-alkyl esters), PMm, and corresponding polyimides.[164)] https://doi.org/10.1038/s41428-020-00458-8

Ishige and co-workers developed a variable temperature (VT) pMAIRS equipment and also a grazing-incidence wide-angle X-ray scattering (GI-WAXS) equipment incorporated with a heating device to analyze molecular orientation changes during heat treatment of polyimide precursor films for making polyimide films.[164] Polyimide is a main-chain type liquid crystalline polymer having rigid main chains, which is widely used in organic devices such as alignment films in liquid crystal displays because of its strong anchoring effect.[166),167] As a polyimide precursor, PM*m*, a fluorinated aromatic diamine-containing polyamide ester with controllable isomerism, was used (Figure 12). PM*m* exhibits a lyotropic liquid crystalline phase in a 50wt% solution of N-methylpyrrolidone, and the polyimide PMDA-TFDB is obtained by heat treatment at 300°C. Spin-coated thin films were prepared from dilute solutions of PM*m,* and changes in molecular orientation during the heat treatment process were analyzed by VT-pMAIRS. In the pMAIRS-IP spectrum of the precursor polyimide film before heating, the C=O stretching vibration of the ester group was identified at 1730 cm^{-1} and the C=O stretching vibration of the amide group at 1670 cm^{-1} (Figure 13).

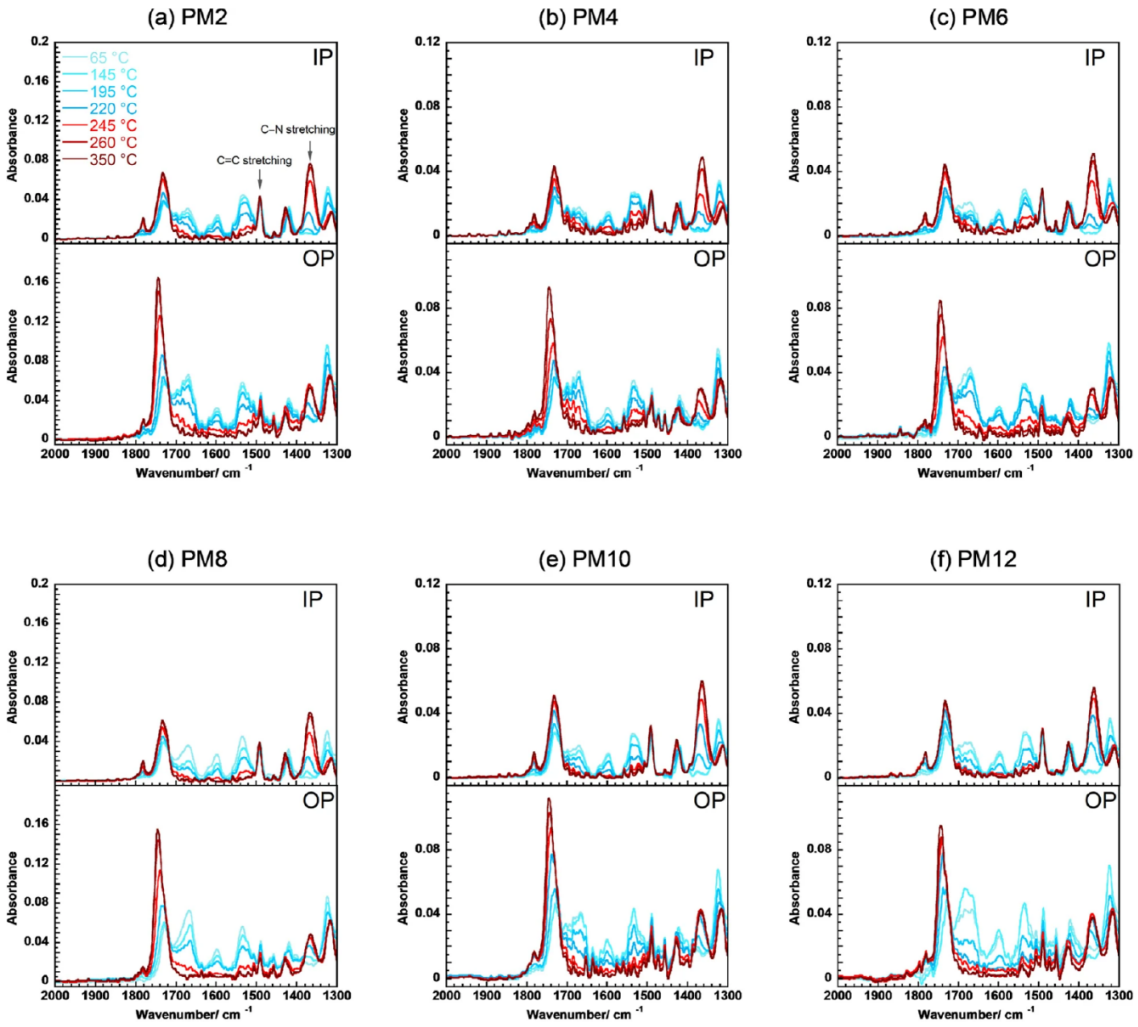

Figure 13 a-f In-plane (IP) and out-of-plane (OP) spectra of PMm (m = 2, 4, 6, 8, 10, and 12) thin films acquired during heating from 65 to 260°C by VT-pMAIRS. The spectra of the films substantially cured at 350°C were obtained at ambient temperature and are represented as 350°C.[164)]
https://doi.org/10.1038/s41428-020-00458-8

On heating, the intensities of these two bands decrease while the intensities of the C=O asymmetric stretching vibration band of the imide ring at 1745 cm^{-1} and the C-N stretching vibration band of the imide group at 1370 cm^{-1}, both of which are originated from the formation of polyimide increase. There was no change in the band intensity of the C=C stretching vibration mode of the aromatic diamine group at 1490 cm^{-1} before and after heating. The imidization rate during the heating process was estimated from the C-N

stretching vibration band intensity of the imide group. Only on the conventional transmission method, it is difficult to estimate the imidization rate because the C-N stretching vibration intensity of imide groups depends not only on the concentration of imide groups but also on their orientation. pMAIRS makes it possible to quantitatively calculate the imidization reaction rate on the useful fact that the average spectrum of the pMAIRS-IP and -OP spectra is constant regardless of orientation as found in Sec. 3.2. The correlation between the imidization rate and the orientation angle shows that the in-plane orientation of the precursor polyimide moiety is higher than that of the polyimide moiety as the temperature increases in the initial stage of imidization, which implies that the overall orientation is inhomogeneous.

The precursor had a higher percentage of the edge-on orientation than polyimide. Comparing the orientation angles obtained from pMAIRS and GI-WAXS, it was found that both precursor and polyimide had a higher percentage of the edge-on orientation, suggesting that the packing of the alkyl side chains in the precursor induces edge-on orientation, but the rotation of the polymer main chain upon imidization reduces the edge-on orientation. Note that pMAIRS yields an averaged orientation angle covering the ordered and disordered regions in a film. The pMAIRS and GI-WAXS results revealed that polyimide begins to be generated in unoriented regions where the precursor has a high mobility, and after that polyimide is further generated in regions where the precursor is strongly oriented in plane.

Ishige and co-workers also studied the changes in imidization rate and orientation ordering in thin films for fully-aromatic polyimides having various main-chain backbones during a heating process using VT-pMAIRS.[163] They showed that the main-chain orientation changes differently depending on the main-chain structure through the imidization reaction.

For the side-chain polymer liquid crystals, similar studies using a combination of MAIRS and XRD are also reported by S. Nagano and co-workers.[168)–171)] From comparison of

pMAIRS spectra with XRD patterns, they revealed the existence of homeotropically oriented regions near the film surface. Thus, by using MAIRS and XRD together, it is possible to discuss the orientation of the liquid crystal throughout the thin film.

3.4 Interstellar Materials Science

Interfacial chemistry has long been recognized to play an important role in the study of interstellar molecules[172], and Hama and co-workers present brilliant works showing that MAIRS is useful for revealing the structure and reactions of adsorbed molecules at an interface.[173–175] The surface of the interstellar dust composed of a variety of solid and liquid materials works as adsorption sites of interstellar molecules. The surface of interstellar dust is covered with various solid-phase molecules, called interstellar icy dust.[176] Many compounds are considered to be generated on the surface of the interstellar dust. Although the cryogenic temperature of 10 K in interstellar space makes it difficult for general chemical reactions to proceed, Watanabe and Hama showed that atoms attached to the surface of interstellar dusts can react through the quantum tunneling effect.[172] In other words, understanding of the thin-film growth and reactions of interstellar molecules is important for understanding the development mechanism of planetary systems.[176,177] Among them, the surface potential of a polar molecule, nitrous oxide (N_2O), is reported to vary a lot with temperature.[178–180] Since nonpolar molecules do not show such a trend,[181,182] they performed MAIRS2 measurements of methane and nitrous oxide deposited on various substrates at cryogenic temperatures to determine their orientation in amorphous thin films composed of these molecules.[173]

Both MAIRS-IP and -OP spectra of methane show a similar intensity at about 3010 cm^{-1}, which is assigned to the asymmetric (called ‘ν3’[183]) C-H stretching vibration mode (Figure 14A), methane molecules with a random orientation increase with deposition time. The

identical ν3 mode gives different wavenumber positions in the MAIRS2-IP and -OP spectra at 3009 cm^{-1} and 3012 cm^{-1}, respectively, which is induced by the TO-LO splitting.[84),184),185)] In the case of oriented N_2O molecules, the band at 2222 cm^{-1} of the MAIRS2-IP spectrum corresponds to the ν3 band of the transmission spectrum.[186)] The band of amorphous N_2O in the MAIRS2-OP spectrum shows, however, a larger wavenumber shift from 2227 cm^{-1} to 2251 cm^{-1} with increasing the deposition thickness (Figure 14B). The intensity of the MAIRS2-OP spectrum is getting larger than that of the MAIRS2-IP one with the deposition time.

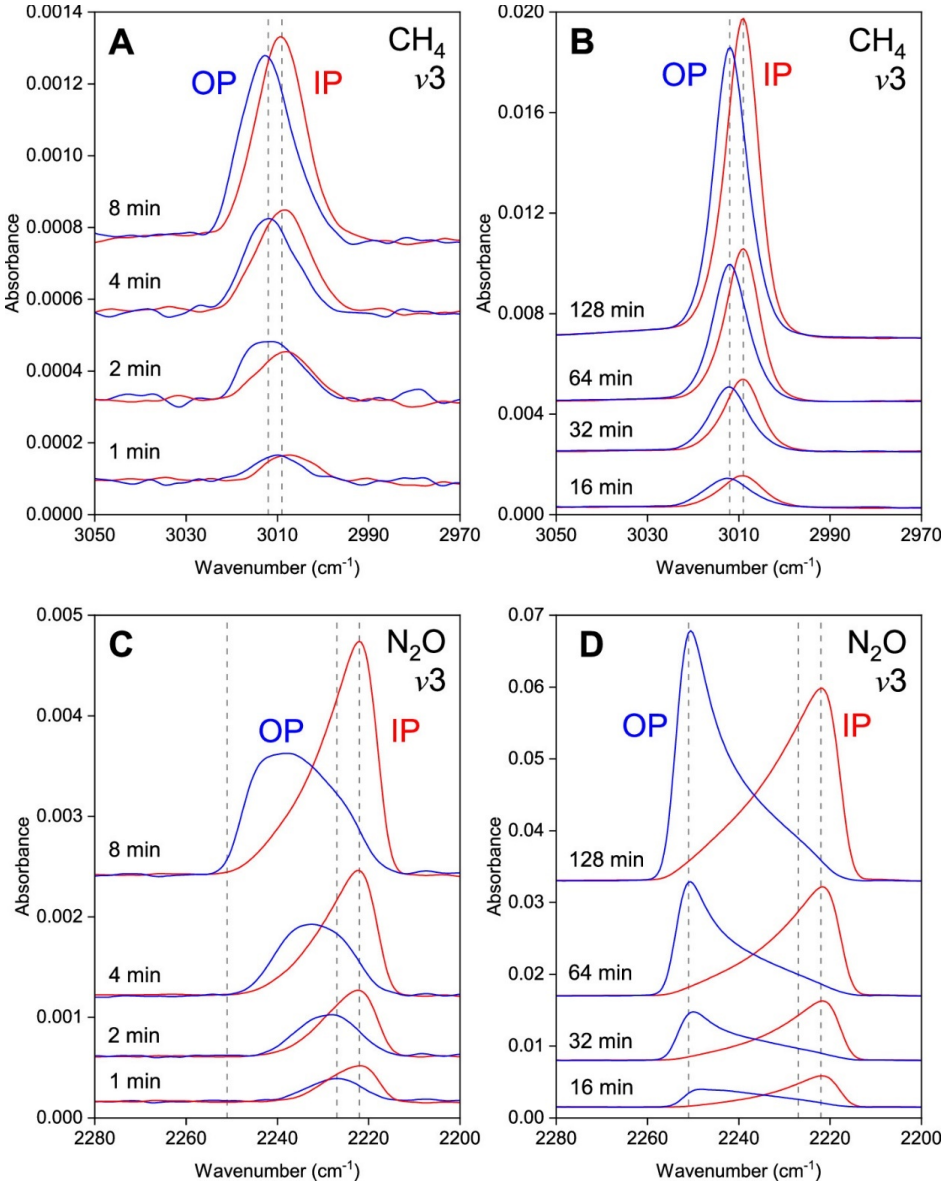

Figure 14 IP and OP spectra obtained by MAIRS2 as a function of gas exposure time. (A and B) ν3 C-H stretching vibration band of amorphous CH_4 at 6 K. The dashed gray guidelines are at 3012 and 3009 cm^{-1}. (C and D) ν3 antisymmetric stretching vibration band of amorphous N_2O at 6 K. The dashed gray guidelines are at 2251, 2227, and 2222 cm^{-1}. The pressure in the chamber is 6.7×10^{-6} and 6.0×10^{-6} Pa during CH_4 and N_2O exposure, respectively.[173)]
https://doi.org/10.1021/acs.jpclett.0c01585

On the other hand, dipole-dipole interactions within amorphous N_2O was suggested to influence the molecular vibrations of the surrounding N_2O.[187)] In addition, the arrangement of dipoles may also cause another wavenumber shift due to the vibrational Stark

effect.[188),189)] Therefore, morphological change of the N_2O layer occurs as deposition proceeded, which significantly distorted the shape and intensity of the MAIRS2-OP spectrum. In other words, the possibility that the shape of the MAIRS2-IP and -OP spectra may change significantly regardless of the molecular orientation of N_2O must be considered.

To determine the orientation angle of N_2O, they focused on the weak ν3 band of $^{14}N^{15}NO$, an isotopomer of N_2O that contains the nitrogen isotope ^{15}N.[190)] This band does not resonate with the ν3 band of $^{14}N_2O$, and its concentration is sufficiently low.[191)] The intermolecular vibrational coupling can thus be neglected. In other words, with the ν3 band of $^{14}N^{15}NO$, we can calculate the molecular orientation angle of $^{14}N^{15}NO$ in amorphous N_2O. No intensity change at 2187 cm^{-1} corresponding to the ν3 band of $^{14}N^{15}NO$, and no wavenumber shift in the MAIRS2-OP spectrum found for $^{14}N_2O$ was observed (Figure 15) as expected. The orientation angle of N_2O in the amorphous N_2O film was then calculated to be 65.1° ± 1.5° from the surface normal. In addition, the MAIRS2 spectra of N_2O deposited after growing amorphous Ar on the silicon substrates are similar to those on a bare silicon substrate, indicating that N_2O shows the same orientation even on amorphous Ar as on a silicon substrate. Thus, the MAIRS2 measurements indicate that the transient mobility of N_2O molecules in the amorphous state by physical adsorption via van der Waals forces determines the molecular orientation on the substrate.

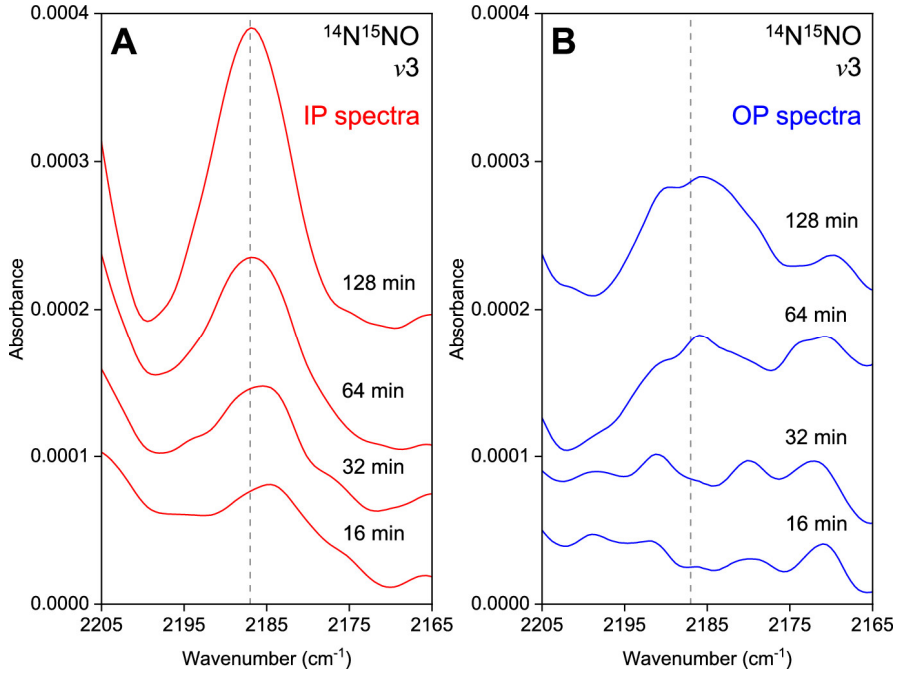

Figure 15 MAIRS2 for solid N_2O at 6 K in the region of the ν3 ($^{14}N^{15}NO$) isotope band as a function of exposure time at 6.0 × 10^{-6} Pa. (A) IP spectra and (B) OP spectra. gray guidelines are at 2187 cm^{-1}.[173] https://doi.org/10.1021/acs.jpclett.0c01585

MAIRS is also used for the study of amorphous ice involved in reactions at the interstellar icy dust interface.[174] On the surface of amorphous ice, there are dangling OH groups with weak hydrogen bonds.[192] The dangling OH groups characterize the amorphous ice. These dangling OH groups work as molecular adsorption sites and catalyze chemical reactions.[193] The dangling OH groups are also useful to quantitatively discuss the porosity and specific surface area of amorphous ice.[194] Hama and co-workers prepared thin films of amorphous ice on a silicon substrate and MAIRS2 spectra were measured at low temperatures to determine the abundance of dangling OH groups.[174] When amorphous ice was grown at 10 K, bands at 3720 cm^{-1} and 3696 cm^{-1} corresponding to two- and three-coordinated dangling OH groups were identified (Figure 16A and B). To simplify the analysis of the dangling OH groups, they readily prepared only the three-coordinated dangling OH groups and produced amorphous ice at 90 K. As a result, only the band at 3696 cm^{-1} increase with the deposition

time, confirming that only three-coordinated dangling OH groups are grown. In addition, the intensity of the OP spectrum is stronger than that of the MAIRS2-IP spectrum (Figure 16 C). It was found that the dangling OH groups are oriented in the OP direction. This reminds us of our another analysis of the perpendicular orientation of dangling OH group bonds of a silicon substrate.[195)]

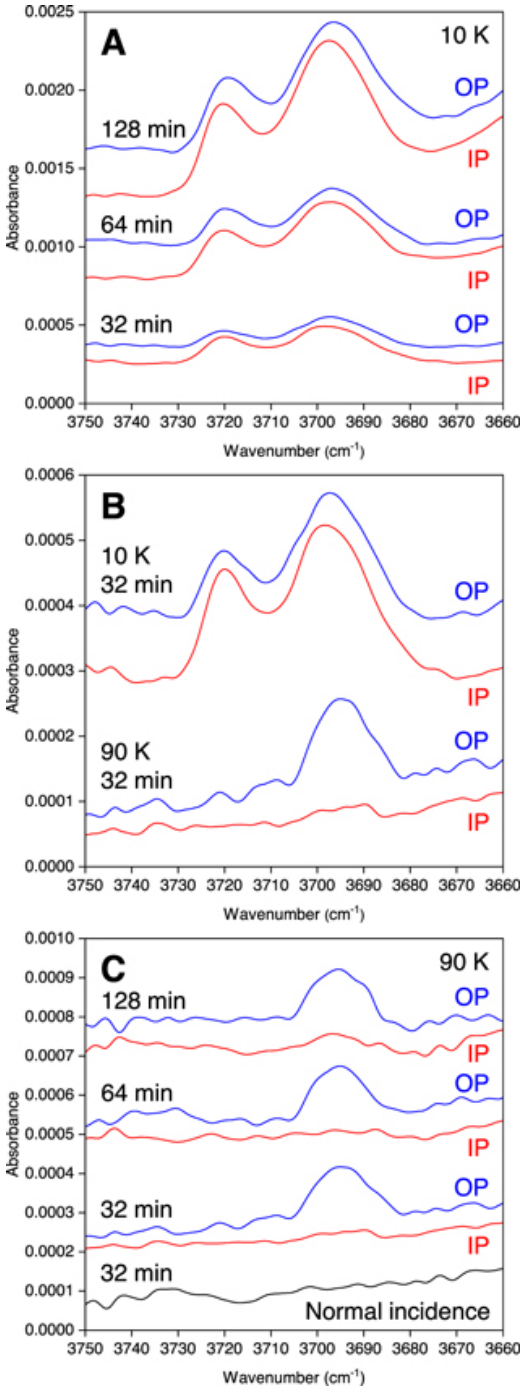

Figure 16 MAIRS2-IP and -OP spectra of amorphous water on a Si substrate at 3750–3660 cm^{-1}. (A) Amorphous water at 10 K as a function of water exposure time. (B) Amorphous water at 10 K and 90 K formed after 32 minutes of water exposure. (C) Amorphous water at 90 K as a function of water exposure time. The pressure in the chamber is 2.2×10^{-6} Pa. The amorphous water samples were prepared using H_2O with 3.5 mol% HDO.[174] DOI 10.3847/2041-8213/ac3a0e

Next, to quantify the amount of dangling OH groups on the amorphous ice surface, MAIRS2 measurements were performed while methanol was exposed to the amorphous ice surface at 90 K. As the exposure time of methanol increased, the 3696 cm^{-1} band of the dangling OH groups disappears and the 1034 cm^{-1} band corresponding to the C–O stretching vibration mode of methanol increases (Figure 17). This band was observed in the MAIRS2-OP spectrum higher than that in the IP one. In other words, the bands of the dangling OH groups disappeared as methanol adsorbed to the dangling OH groups on the amorphous ice surface. The amount of dangling OH groups can approximately be assumed to be the amount of methanol that can be estimated from the decrease of dangling OH groups, the amount of dangling OH groups on the amorphous ice surface was calculated to be $3.3 \pm 0.6 \times 10^{13}$ molecules cm^{-2}. The ice crystal surface contains 1.0×10^{15} molecules cm^{-2} of water molecules, and[196] about half of them are supposed to form the dangling OH groups. Since the amorphous ice surface contains the same amount of water molecules as the ice crystal surface, the MAIRS analysis indicates that the dangling OH groups on the amorphous ice surface have a portion of only 3%.

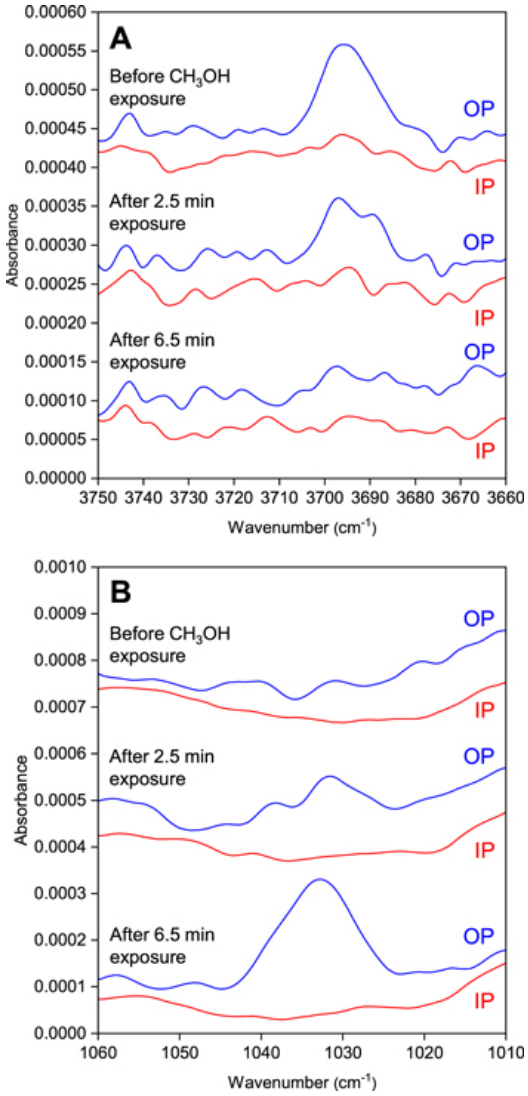

Figure 17 MAIRS2-IP and -OP spectra of amorphous water on a Si substrate at 90 K as a function of CH_3OH exposure time. (A) 3750–3660 cm^{-1} for the dangling-OH peak and (B) 1060–1010 cm^{-1} for the CO stretching band of CH_3OH. Amorphous water was prepared at 90 K by 32 minutes of water exposure (H_2O with 3.5 mol% HDO) at 2.2×10^{-6} before CH3OH exposure. The pressure in the chamber is 2.2×10^{-8} Pa during CH_3OH exposure.[174] DOI 10.3847/2041-8213/ac3a0e

3.5 Medical applications using ZnO nanowire

Analysis of the adsorption process of molecules on the surface of 'nanowires' is another remarkable example of the application of MAIRS.[197] Oxide nanowires represented by ZnO are expected for sensor materials because they can detect molecular adsorption in the liquid and gas phases giving electrical signals.[198),199] However, the mechanism of molecular

adsorption on solid surfaces, including oxides, is still largely unexplored, since it is difficult to measure the presence or absence of adsorbates on solid surfaces mostly due to limitations in measurement sensitivity. The mechanism of molecular adsorption on solid surfaces is still largely unknown because it is difficult to measure the presence or absence of adsorption on the solid surface itself due to the limitation of measurement sensitivity. IR spectroscopy is extremely sensitive in terms of sensitivity, and when combined with the MAIRS technique, it greatly contributes to the analysis of molecular adsorption processes on solid surfaces.

Wang and co-workers discussed the adsorption mechanism of nonanal on the surface of ZnO nanowires using IR spectroscopy.[200] Nonanal (Figure 18b) is found in the exhaled breath of certain cancer patients, and it is tried to be detected by using the surfaces of oxide nanowires.[201–203] IR spectroscopy combined with XPS showed that heat treatment of ZnO nanowires decreases the OH groups on their surface and the amount of nonanal adsorbed also decreases.[204] This means that nonanal would be adsorbed on the OH groups or the Zn^{2+} sites on the ZnO nanowire surface.

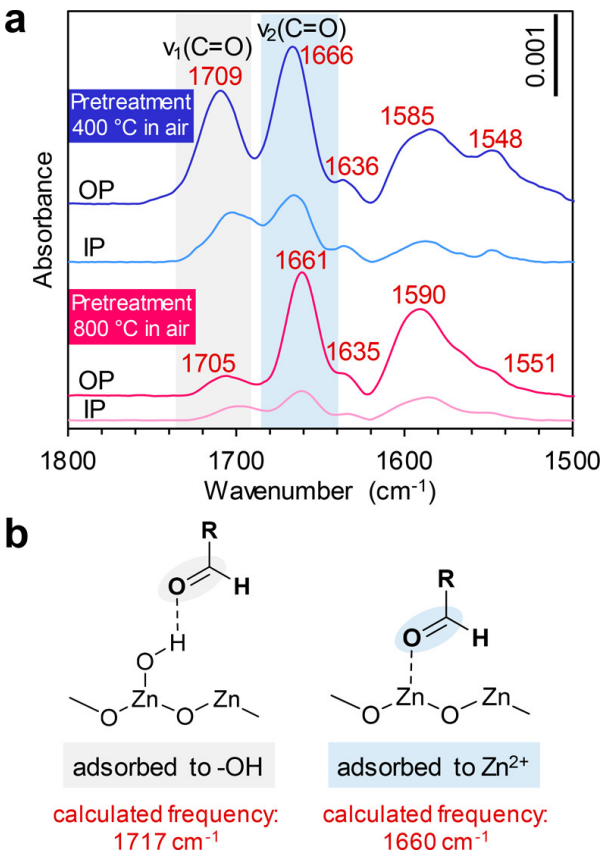

Figure 18 (a) pMAIRS spectra (1770–1620 cm^{-1}) of nonanal adsorbed on ZnO nanowires pretreated at 400°C (blue line) or 800°C (red line) in air. (b) Schematic structures of surface-adsorbed nonanal and corresponding DFT-calculated C=O frequencies.[200] https://doi.org/10.1021/acs.nanolett.8b05180

Then, the adsorption process of nonanals on the surface of ZnO nanowires was investigated by pMAIRS. Note that in the case of ZnO nanowires, needles growing perpendicular to the plate work as substrates, and each needle surface is perpendicular to the plate surface. As a result, the concept of the IP and OP directions is reversed. Nonanal adsorbed on the ZnO nanowires heated at 400°C exhibits bands at 1709 and 1666 cm^{-1} (denoted as ν_1 and ν_2 respectively) in the pMAIRS-OP spectra (Figure 18a) that is associated with the C=O stretching vibration (ν(C=O)) mode. By comparing to the IR spectrum of nonanal in the liquid phase, the ν_1(C=O) and ν_2(C=O) bands are attributed to adsorption on the ZnO surface OH groups and Zn^{2+} sites, respectively, which is supported by the DFT

calculations.

The strong pMAIRS-OP spectral intensities of both ν_1(C=O) and ν_2(C=O) bands indicate that the C=O groups adsorb parallel to the ZnO nanowire surface, as shown in Figure 18b. When the pMAIRS intensity ratio, OP/IP, are compared, the ratio of the ν_2 band is larger than that of the ν_1 band. This result is also consistent with the fact that the Zn^{2+}-coordination sites are fixed nearly perpendicularly to the plate surface.[205] Comparing the intensity ratio, ν_2(C=O)/ν_1(C=O), for the samples heat-treated at 400°C and 800°C, the ratio gets significantly lower at 800°C. This agrees with the former result of the reduced OH groups on the surface of ZnO nanowires after the heat-treatment at 800°C studied by IR and XPS. In this manner, the pMAIRS measurements reveal the details of nonanal adsorption to the OH groups and Zn^{2+}-coordination sites on the ZnO nanowire surface.

As a practical application of the combination of the ZnO nanowires and pMAIRS techniques, Yasui and co-workers developed a new highly sensitive technique to detect extracellular vesicles specific to ovarian cancer with high accuracy by adsorbing and separating extracellular vesicles on ZnO nanowires.[206] Since various substances as well as the target extracellular vesicles, such as proteins in blood plasma, are all adsorbed on the ZnO surfaces, polyketone was coated on the nanowires (Figure 19). Polyketone is of a monomer of 3,3-dimethylpentane-2,4-dione, and the number of ketone units can be controlled at our will so that the balance of hydrophobicity/hydrophilicity can also be controlled.[207),208] When the nanowire surfaces are covered with polyketone, the carbonyl groups are more likely to interact with extracellular vesicles than with proteins. The molecular orientation and adsorption behavior of polyketone on the surfaces were investigated by pMAIRS.

In the pMAIRS-IP and -OP spectra of ZnO nanowires coated with dimers of polyketone,

the carbonyl stretching vibration bands are observed at 1695 cm^{-1} and 1697 cm^{-1}, respectively (Figure 19B). DFT calculations indicate that the band at 1695 cm^{-1} is due to the carbonyl group coordinated with Zn, while the band at 1697 cm^{-1} is of a free carbonyl group facing outward the plane surface. The carbonyl groups strongly coordinated with Zn are almost perpendicular to the nanowire surface, resulting in a strong band solely in the 'IP' spectrum. On the other hand, the free carbonyl groups are weakly interacted with the nanowire surface resulting in a tilted orientation, and therefore it also gives an OP band as well as the IP one. The intensity ratio of the IP band to the OP one decreases as the number of carbonyl groups increases. This confirms that the number of free carbonyl groups increases when the molecule becomes more chained (Figure 19C, D).

Free carbonyl groups would favorite binding to extracellular vesicles. Indeed, when extracellular vesicles were adsorbed on polyketon-coated ZnO nanowires and then recovered by introducing phospholipids that is more acidic than polyketones, the recovery of extracellular vesicles was higher in the dimer and 16-mer-coated systems than in the polydisperse polyketon-coated system or by centrifugation (Figure 19F). Furthermore, the purity of the recovered extracellular vesicles was higher in the 16-mer polyketon than in the dimeric and polydisperse systems (Figure 19H). In other words, as supported by the results of pMAIRS, the 16-mer polyketon with more free carbonyl groups suppressed the adsorption of proteins on the surface of ZnO nanowires, resulting in selective adsorption of extracellular vesicles, and the introduction of phospholipids into them allowed the recovery of highly pure extracellular vesicles. The results show that extracellular vesicles are selectively adsorbed and that highly pure extracellular vesicles would be recovered by introducing phospholipids.

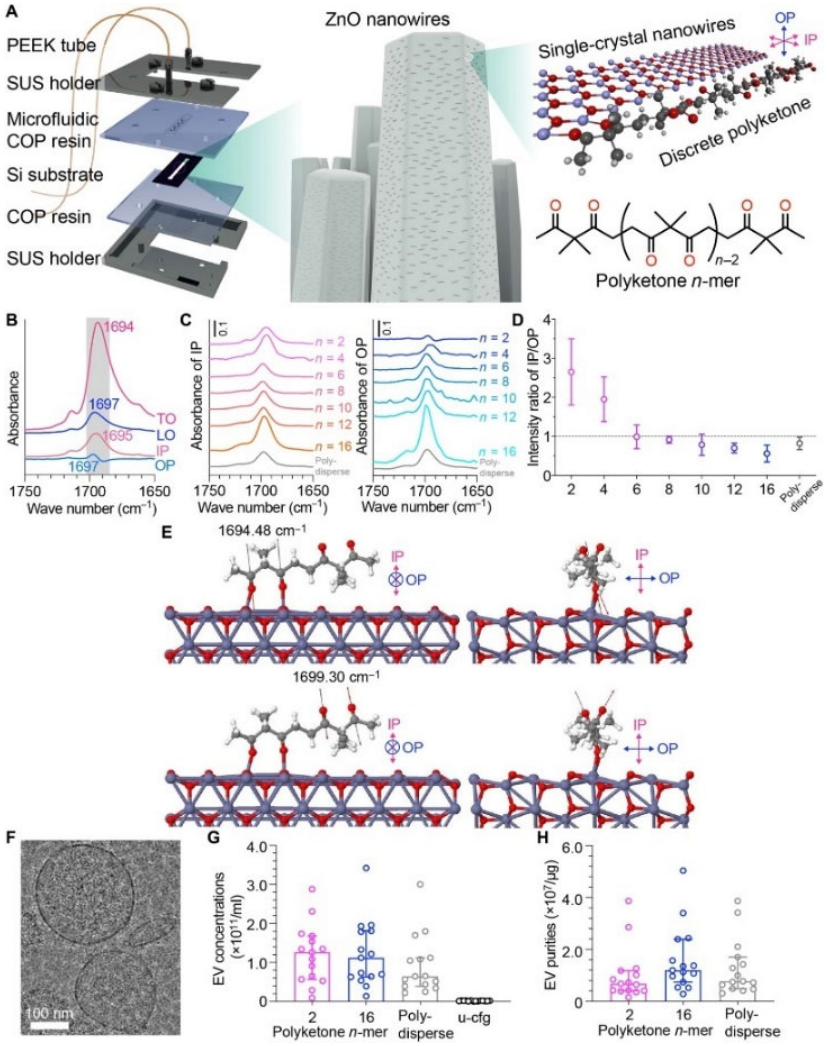

Figure 19 Surface modification of single-crystal ZnO nanowires by polyketone. A) Schematic illustrations for the device setup and ZnO nanowire s modified by polyketone. (B) The TO and LO spectra of polyketone 2-mer converted from ATR spectra; The TO and LO spectra reproduce the pMAIRS-IP and -OP spectra, respectively, confirming the pMAIRS The TO and LO spectra correspond to the IP and OP spectra, respectively, confirming the pMAIRS measurements are correctly done. The gray box indicates the wave number range of the C=O stretching vibration bands. (C) pMAIRS-IP and -OP spectra of polyketones with different lengths. The bottom spectrum named "Polydisperse" is of the polyketone synthesized with unaligned lengths (mean, 9.5-mer). (D) Ratio of the IP intensity to the OP one; the OP and IP intensities used for the ratio were given in (C). (E) Stable structures of polyketone 2-mer attached to ZnO nanowires predicted by DFT calculations. The black arrows and numbers indicate the direction of the vibrational stretching mode and the wavenumber, respectively. In (A) and (E), the arrows marked by OP and IP indicate the directions of the polarization distribution during the pMAIRS measurement. (F) Cryo-TEM image of extracellular vesicles (EVs) recovered from serum by the ZnO (G) Concentrations of EVs recovered from serum by the ZnO nanowires modified with polyketone 2-mer, 16-

mer, and the polydisperse, and collected by ultracentrifugation (u-cfg). (H) Purities of EVs recovered in serum by the ZnO nanowires modified with polyketone 2-mer and 16-mer, and the polydisperse.[206)]
https://doi.org/10.1126/sciadv.ade6958

3.5 Phonon analysis by MAIRS

As found in the former sections, MAIRS basically provides the function of molecular orientation analysis. If this function is reconsidered as the analysis of optical anisotropy in thin films, an additional function is figured out than the orientation analysis.

As a matter of fact, IR spectra consists of not only the normal-mode bands in a single molecule, but also coupled-oscillation bands, i.e., phonon bands. In inorganic matters, let us take an example of ionic crystals represented by sodium chloride, sodium and chloride ions are alternatively and repeatedly located and they are combined by mostly homogeneous interactions of the ionic interactions (Figure 20a). In this case, the concept of a single molecule is for nothing, and the coupled oscillation over the crystal is the normal mode.[209)]

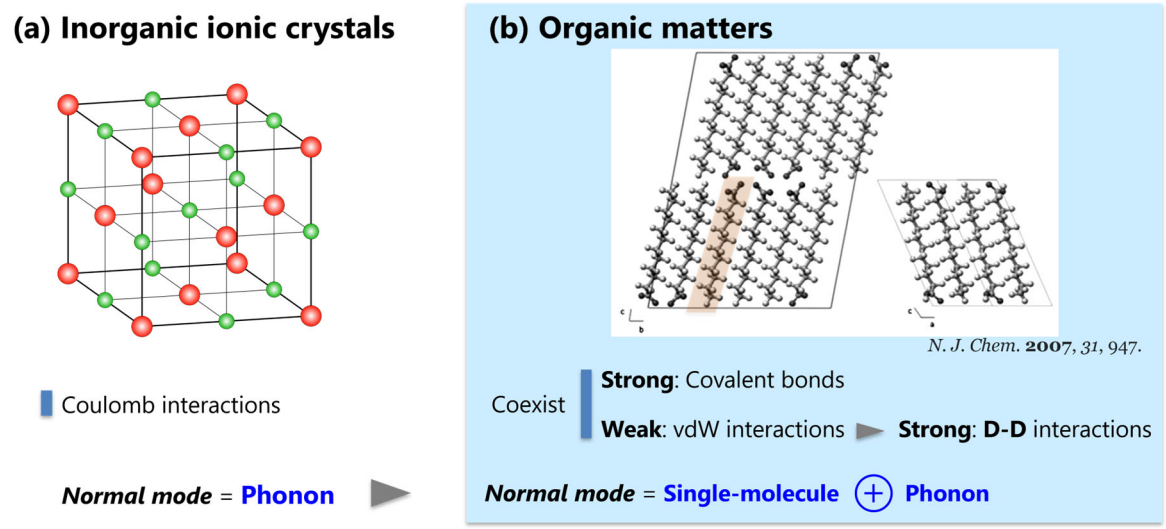

Figure 20 Schematics for understanding of normal modes in (a) inorganic and (b) organic matters.

On the other hand, in organic matters, organic molecules are weakly packed with a very weak interactive forces of van der Waals force represented by London's dispersion force,

while the individual molecule consists of atoms connected by the strongest bond of the covalent bond (Figure 20b). In other words, two largely different interactive forces coexist in the matter. In the organic matters, therefore, the normal mode is mostly defined for each single molecule, and the coupled oscillations over the molecules can be ignored. However, if the molecule has chemical groups having a large permanent dipole moment such as the C=O and C−F bonds, the intermolecular interactions cannot be ignored, and the coupled-oscillation (phonon) bands appears with a similar shape to the single-molecular vibration bands. Here, we have a problem that the phonon mode in a thin film has a character that the transition moment is largely oriented to the surface-perpendicular direction, which is known as Berreman's effect.[84),86),209)–211)] Therefore, if the phonon mode is recognized as the normal single-molecular mode in a wrong manner, discussion of the molecular orientation would go to a wrong direction.

To avoid the wrong discussion, discrimination of the phonon bands from the normal IR absorption bands is critically important. Since the Berreman mode has a unique character that the transition moment is perpendicular to the film surface irrespective of the molecular orientations, the function of the anisotropic analysis of MAIRS works powerfully.

Figure 21 presents IR MAIRS spectra of 5-monolayer LB film of cadmium stearate deposited on a Ge substrate.[80)] The spectra have basically the same shape for both IP and OP spectra as found in the transmission and RA spectra, respectively. In the high wavenumber region, both ν_aCH_2 and ν_sCH_2 bands appear at the almost the same position for both IP and OP spectra, respectively, which means that the normal alkyl (CH) groups show no phonon character.

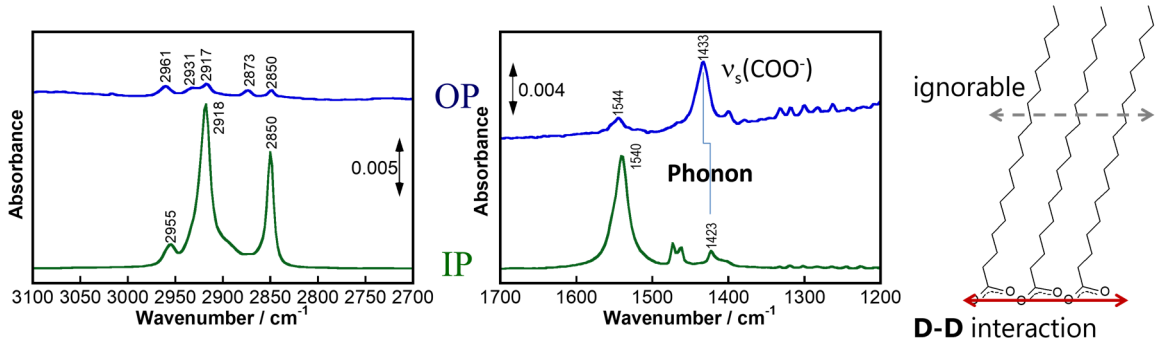

Figure 21 IR MAIRS spectra of 5-monolayer LB film of cadmium stearate on Ge[80)]

On the other hand, in the low wavenumber region, $\nu_s COO^-$ band appears at 1423 cm^{-1} in the IP spectrum while it appears at 1433 cm^{-1} in the OP one. This clear band shift of 10 cm^{-1} is given by the dipole-dipole (D-D) interaction of the COO^- groups in neighboring molecules, which is phonon. A similar thing happens for the $\nu_a COO^-$ band at ca. 1540 cm^{-1}, but the shift is smaller than the symmetric one. This is because the Berreman effect appears stronger for the surface-perpendicular orientation.

Phonon comprises the bulk and surface modes, and if the thickness of the matter is decreased, the portion of the surface mode becomes larger. Figure 22 shows IR ATR spectra of perfluoroalkanes with time.[212)]

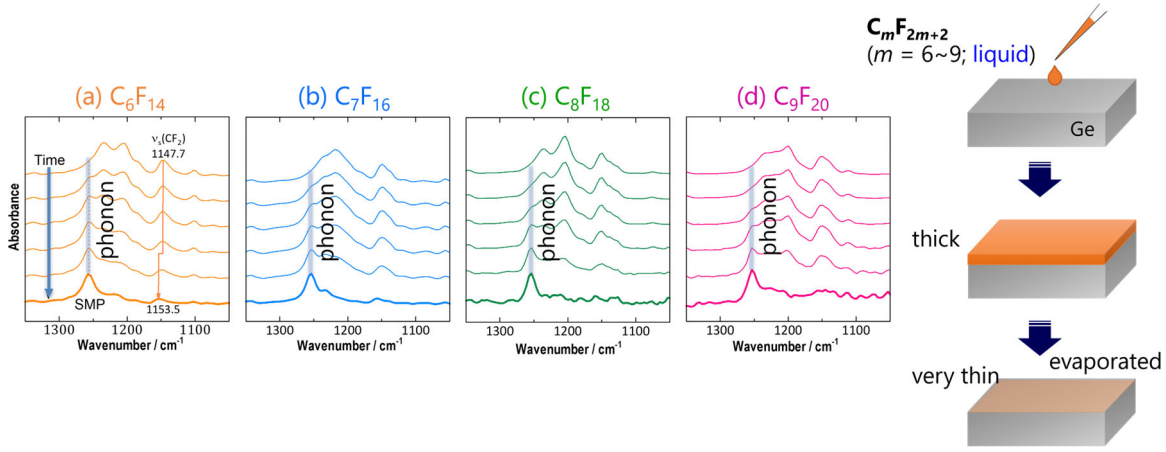

Figure 22 IR ATR spectra of perfluoroalkanes (C_nF_{2m+2}; m = 6~9) on Ge with time.

When the liquid sample is evaporated to be thinner, a new band governs the spectra for

every chain length. The new band is the surface mode of phonon. In particular, just before the full evaporation, the continuous film come apart to gives many particles having a large surface area. In this manner, phonon-relevant bands look like normal IR absorption bands, and they are quite difficult to discriminate from each other.

To discuss the degree of phonon generation, four compounds are prepared named F*n*F*n*-DMPC.[209] They commonly have a skeleton of DMPC (1,2-Dimyristoyl-sn-glycero-3-phosphorylcholine), and the two tail chains are partly replaced by R_f groups with different chain lengths of n = 4 or 8 (F*n*F*n*). If only one chain is replaced, the compound is a hybrid compound (F*n*F0). Note that if the chain length is C8 or longer, the chains are spontaneously aggregated.[213),214)]

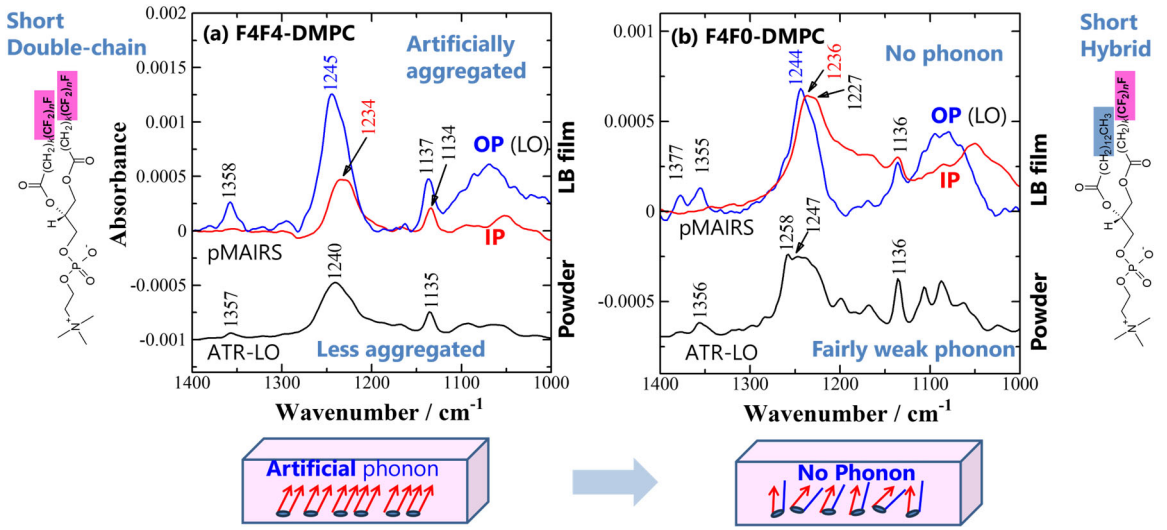

Figure 23 IR MAIRS spectra of a single-monolayer LB film of (a) F4F4-DMPC and (b) F4F0-DMPC on Si. As a reference, the ATR-LO spectrum of the powder sample is also presented.[209]

The LB film of F4F4 exhibits the same mode at different positions of 1234 and 1245 cm^{-1} for IP and OP, respectively, with different strength (Figure 23a). This is a typical Berreman mode, which is readily revealed by MAIRS. If the compound is changed to F4F0, the two bands appear at nearly the same position with the same strength indicating the phonon is

obstructed by inserting the hydrocarbon chain (Figure 23b). Here, the reader may consider that the length of $n = 4$ is too short to aggregate spontaneously. In this case, the monolayer is compressed 'artificially' by the Langmuir technique, and as a result the phonon band is generated. To explore the molecular self-aggregation, the IR spectrum of the powder sample should be visited. As found in the ATR-LO spectrum of the powder sample of F4F4, the spectrum has a similar shape to the MAIRS-OP spectrum. Since the phonon bands are observed as Berreman' modes, they should appear in the OP spectrum. Therefore, this similarity indicates that F4F4 molecules are fairly aggregated even in the powder sample, which suggests that such short R_f chains are aggregated to generate clusters.

On the other hand, as for F4F0, the ATR-LO spectrum has a different shape of the summation (or averaged) of the MAIRS-IP and OP spectra. If the phonon generation is completely obstructed in powder, the spectrum should be close to the IP spectrum. Therefore, the average spectrum indicates that even the hybrid chains of the R_f and alkyl chains also generates the clustering to some extent.

Similar experiments are performed for F8F8 and F8F0. As found in Figure 24, F8F8 exhibits a phonon mode at 1250 cm^{-1}, but it is annihilated for F8F0, which is common to F4F*m*. Of interest is that both powder spectra show similar shape to that of the MAIRS-OP spectrum for each case. This implies that the long R_f chains are very strongly aggregated spontaneously even for the hybrid compound. This results indicates, therefore, that the R_f chains as the side chains of a polymer, often make clustering in an inhomogeneous manner.[215] This means that the phonon analysis using MAIRS is powerful to analyze the side R_f chains in polymers.

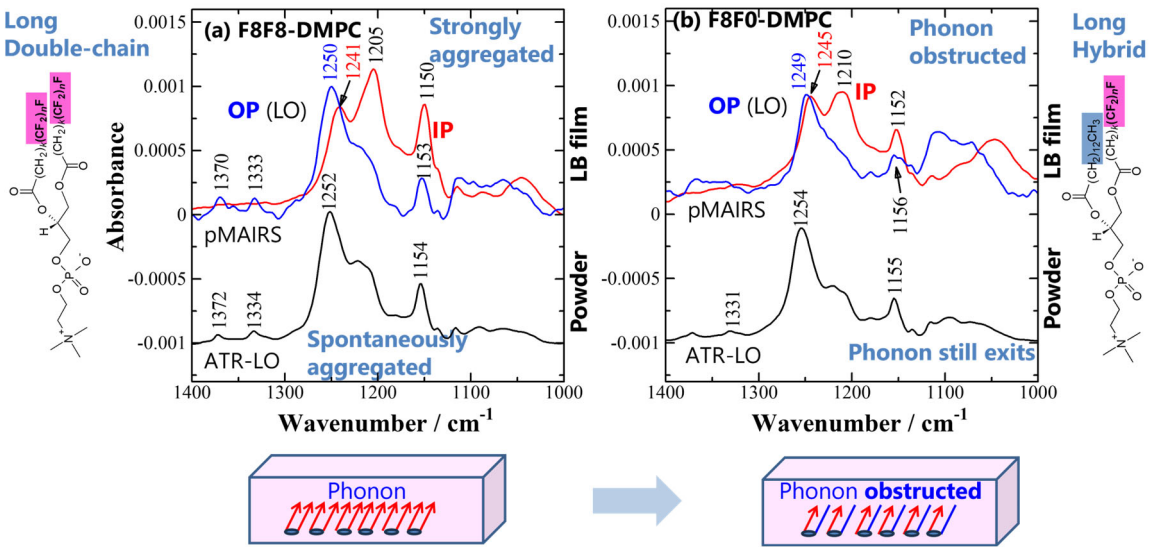

Figure 24 IR MAIRS spectra of a single-monolayer LB film of (a) F8F8-DMPC and (b) F8F0-DMPC on Si. As a reference, the ATR-LO spectrum of the powder sample is also presented.[209)]

4. Conclusions

This review shows that the MAIRS technique coupled with IR spectroscopy works powerfully to reveal not only the quantitative molecular orientation at individual chemical groups, but for quantitative analysis of chemical reaction, cross-section of IR absorption and phonon. One of the most useful aspects of the technique is that the analysis can be performed for films having uneven surfaces prepared by practical techniques of spin-coating and dip-coating ones. In addition, MAIRS covers both crystalline and amorphous regions in thin films. Therefore, MAIRS is now recognized to be equivalent and complement to the diffraction techniques such as X-ray and electron diffractions. Since most of the polymer matters have amorphous regions, MAIRS would soon be recognized as an essentially useful technique for polymer science in the future.

Acknowledgments

This work was supported by a Grant-in-Aid Challenges in Research (Exploratory) (No. 22H02106 (TH)), Grant-in-Aid for Scientific Research (S) (No. 23H05459 (KA)), Grant-in-Aid for Scientific Research (A) (No. 20H00392 (KA)), Grant-in-Aid for Scientific Research (B) (No. 23K23374 (TH)), Grant-in-Aid for Scientific Research (C) (No. 23K04703 (TM)) and Grant-in-Aid for Early-Career Scientists (No. 22K14604 (NS)) from the Japan Society

for the Promotion of Science (JSPS), and the Asahi Glass Foundation (TH) to which the authors' thanks are due.

References:

1) M. Sugiyama, M. Akiyama, Y. Yonezawa, K. Komaguchi, M. Higashi, K. Nozaki and T. Okazoe, Science **377** [6607], 756 (2022).

2) K. Hirano, Bull. Chem. Soc. Jpn. **96** [3], 198 (2023).

3) H. Zhang, T. Watanabe, M. Okumura, M. Haruta and N. Toshima, Nat. Mater. **11** [1], 49 (2012).

4) N. Kito, S. Takano, S. Masuda, K. Harano and T. Tsukuda, Bull. Chem. Soc. Jpn. **96** [9], 1045 (2023).

5) E. Yashima, K. Maeda and Y. Okamoto, Nature **399** [6735], 449 (1999).

6) Y. Furukawa and D. Shimokawa, Bull. Chem. Soc. Jpn. **96** [11], 1243 (2023).

7) S. Datta, Y. Kato, S. Higashiharaguchi, K. Aratsu, A. Isobe, T. Saito, D. D. Prabhu, Y. Kitamoto, M. J. Hollamby, A. J. Smith, R. Dalgliesh, N. Mahmoudi, L. Pesce, C. Perego, G. M. Pavan and S. Yagai, Nature **583** [7816], 400 (2020).

8) T. Matsuno and H. Isobe, Bull. Chem. Soc. Jpn. **96** [5], 406 (2023).

9) R. Matsuda, R. Kitaura, S. Kitagawa, Y. Kubota, R. V. Belosludov, T. C. Kobayashi, H. Sakamoto, T. Chiba, M. Takata, Y. Kawazoe and Y. Mita, Nature **436** [7048], 238 (2005).

10) S. Horike, Bull. Chem. Soc. Jpn. **96** [9], 887 (2023).

11) G. Chen, F. Sciortino, K. Takeyasu, J. Nakamura, J. P. Hill, L. K. Shrestha and K. Ariga, Chem. Asian J. **17** [20], e202200756 (2022).

12) T. Adschiri, S. Takami, M. Umetsu, S. Ohara, T. Naka, K. Minami, D. Hojo, T. Togashi, T. Arita, M. Taguchi, M. Itoh, N. Aoki, G. Seong, T. Tomai and A. Yoko, Bull. Chem. Soc. Jpn. **96** [2], 133 (2023).

13) X. Z. Yu, W. Koshibae, Y. Tokunaga, K. Shibata, Y. Taguchi, N. Nagaosa and Y. Tokura, Nature **564** [7734], 95 (2018).

14) N. Kasuya, J. Tsurumi, T. Okamoto, S. Watanabe and J. Takeya, Nat. Mater. **20** [10], 1401 (2021).

15) M. Shikida, Y. Hasegawa, M. S. A. Farisi, M. Matsushima and T. Kawabe, Jpn. J. Appl. Phys. **61** [SA], SA0803 (2022).

16) K. Watanabe, Jpn. J. Appl. Phys. **62** [1], 010507 (2023).

17) D. L. Goldfarb, Jpn. J. Appl. Phys. **61** [SD], SD0802 (2022).

18) T. Yanagida, T. Kato, D. Nakauchi and N. Kawaguchi, Jpn. J. Appl. Phys. **62** [1], 010508 (2023).

19) J.-S. Ro, H.-M. An and H.-L. Park, Jpn. J. Appl. Phys. **62** [SE], SE0801 (2023).

20) Y. Qin, Z. Wang, K. Sasaki, J. Ye and Y. Zhang, Jpn. J. Appl. Phys. **62** [SF], SF0801 (2023).

21) Y. Sugimoto, P. Pou, M. Abe, P. Jelinek, R. Pérez, S. Morita and Ó. Custance, Nature **446** [7131], 64 (2007).

22) S. Kawai, O. J. Silveira, L. Kurki, Z. Yuan, T. Nishiuchi, T. Kodama, K. Sun, O. Custance, J. L. Lado, T. Kubo and A. S. Foster, Nat. Commun. **14** [1], 7741 (2023).

23) K. Kimura, K. Miwa, H. Imada, M. Imai-Imada, S. Kawahara, J. Takeya, M. Kawai, M. Galperin and Y. Kim, Nature **570** [7760], 210 (2019).

24) Y. Hashikawa and Y. Murata, Bull. Chem. Soc. Jpn. **96** [9], 943 (2023).

25) T. Murata, K. Minami, T. Yamazaki, T. Sato, H. Koinuma, K. Ariga and N. Matsuki, Bull. Chem. Soc. Jpn. **96** [1], 29 (2022).

26) S. devi K. Sundaram, Md. M. Hossain, M. Rezki, K. Ariga and S. Tsujimura, Biosensors **13** [12], 1018 (2023).

27) Z. Zhuang, D. Iida and K. Ohkawa, Jpn. J. Appl. Phys. **61** [SA], SA0809 (2022).

28) Y. Saito, H. Sasabe, H. Tsuneyama, S. Abe, M. Matsuya, T. Kawano, Y. Kori, T. Hanayama and J. Kido, Bull. Chem. Soc. Jpn. **96** [1], 24 (2023).

29) P. A. Shinde, Q. Abbas, N. R. Chodankar, K. Ariga, M. A. Abdelkareem and A. G. Olabi, J. Energy Chem. **79**, 611 (2023).

30) H. Imahori, Bull. Chem. Soc. Jpn. **96** [4], 339 (2023).

31) X. Jia, J. Chen, W. Lv, H. Li and K. Ariga, Cell Rep. Phys. Sci. **4** [2], 101251 (2023).

32) L. T. B. Nguyen and M. Abe, Bull. Chem. Soc. Jpn. **96** [9], 899 (2023).

33) K. Ariga, X. Jia, J. Song, J. P. Hill, D. T. Leong, Y. Jia and J. Li, Angew. Chem. Int. Ed. **59** [36], 15424 (2020).

34) W. Chaikittisilp, Y. Yamauchi and K. Ariga, Adv. Mater. **34** [7], e2107212 (2022).

35) R. P. Feynman, Eng. Sci. **5** [23], 32 (1960).

36) M. Roukes, Sci. Am. **285** [3], 48 (2001).

37) K. Ariga and M. Aono, Jpn. J. Appl. Phys. **55** [11], 1102A6 (2016).

38) K. Ariga, Nanoscale Horiz. **6** [5], 364 (2021).

39) K. Ariga, J. Li, J. Fei, Q. Ji and J. P. Hill, Adv. Mater. **28** [6], 1251 (2016).

40) K. Ariga, M. Nishikawa, T. Mori, J. Takeya, L. K. Shrestha and J. P. Hill, Sci. Technol. Adv. Mater. **20** [1], 51 (2019).

41) G. Moghadam, F. Banisharif, D. Ali, A. H. Reshak and M. M. Ramli, Phys. B: Condens. Matter **647**, 414386 (2022).

42) R. Hikichi, Y. Tokura, Y. Igarashi, H. Imai and Y. Oaki, Bull. Chem. Soc. Jpn. **96** [8], 766 (2023).

43) A. Lorenzo, W. A. Marmisollé, E. M. Maza, M. Ceolín and O. Azzaroni, Phys. Chem. Chem. Phys. **20** [11], 7570 (2018).

44) M. P. Pileni, Phys. Chem. Chem. Phys. **24** [23], 14140 (2022).

45) A. Nayak, S. Unayama, S. Tai, T. Tsuruoka, R. Waser, M. Aono, I. Valov and T. Hasegawa, Adv. Mater. [DOI:10.1002/adma.201703261].

46) M. Eguchi, A. S. Nugraha, A. E. Rowan, J. Shapter and Y. Yamauchi, Adv. Sci. **8** [14], 2100539 (2021).

47) X. Shen, J. Song, C. Sevencan, D. T. Leong and K. Ariga, Sci. Technol. Adv. Mater. **23** [1], 199 (2022).

48) R. Chang, L. Zhao, R. Xing, J. Li and X. Yan, Chem. Soc. Rev. **52** [8], 2688 (2023).

49) G. Chen, F. Sciortino and K. Ariga, Adv. Mater. Interfaces [DOI:10.1002/admi.202001395].

50) G. Chen, S. K. Singh, K. Takeyasu, J. P. Hill, J. Nakamura and K. Ariga, Sci. Technol. Adv. Mater. **23** [1], 413 (2022).

51) G. Chen, B. N. Bhadra, L. Sutrisno, L. K. Shrestha and K. Ariga, Int. J. Mol. Sci. **23** [10], 5454 (2022).

52) Y. Sasaki, X. Lyu, T. Kawashima, Y. Zhang, K. Ohshiro, K. Okabe, K. Tsuchiya and T. Minami, RSC Adv. **14** [8], 5159 (2024).

53) T. Tsuchiya, T. Nakayama and K. Ariga, Appl. Phys. Express **15** [10], 100101 (2022).

54) K. Lee, M. Han, G. Kwon, Y. Jeon, J. Kim and J. You, Appl. Surf. Sci. **613**, 155955 (2023).

55) P. A. Shinde, N. R. Chodankar, H.-J. Kim, M. A. Abdelkareem, A. A. Ghaferi, Y.-K. Han, A. G. Olabi and K. Ariga, ACS Energy Lett. **8** [10], 4474 (2023).

56) R. Samantray, K. Manickavasakam, Vivekanand, B. Pradhan, M. Kandasamy, S. C. Mishra, I. I. Misnon and R. Jose, Mater. Chem. Phys. **314**, 128885 (2024).

57) D. Barreca and C. Maccato, CrystEngComm **25** [28], 3968 (2023).

58) N. Agamendran, M. Uddin, M. S. Yesupatham, M. Shanmugam, A. Augustin, T. Kundu, R. Kandasamy, K. Sasaki and K. Sekar, Langmuir **40** [7], 3320 (2024).

59) W. Hu, J. Shi, W. Lv, X. Jia and K. Ariga, Sci. Technol. Adv. Mater. **23** [1], 393 (2022).

60) L. Sutrisno and K. Ariga, NPG Asia Mater. **15** [1], 21 (2023).

61) R. B. Laughlin and D. Pines, Proc. Natl. Acad. Sci. **97** [1], 28 (2000).

62) K. Ariga and R. Fakhrullin, Bull. Chem. Soc. Jpn. **95** [5], 774 (2022).

63) K. Ariga, Bull. Chem. Soc. Jpn. **97** [1], uoad001 (2023).

64) K. Ariga, Chem. Mater. **35** [14], 5233 (2023).

65) K. Ariga, J. Song and K. Kawakami, Chem. Commun. **60** [16], 2152 (2024).

66) Y. Kawasaki, M. Nakagawa, T. Ito, Y. Imura, K.-H. Wang and T. Kawai, Bull. Chem. Soc. Jpn. **95** [7], 1006 (2022).

67) Z. Zhang, R. Zhu, Y. Tang, Z. Su, S. Hu, X. Zhang, J. Zhang, J. Zhao, Y. Xue, X. Gao, G. Li, J. Pascual, A. Abate and M. Li, Adv. Mater. e2312264 (2024).

68) O. N. Oliveira, L. Caseli and K. Ariga, Chem. Rev. **122** [6], 6459 (2022).

69) S. Negi, M. Hamori, Y. Kubo, H. Kitagishi and K. Kano, Bull. Chem. Soc. Jpn. **96** [1], 48 (2022).

70) G. Decher, Science **277** [5330], 1232 (1997).

71) K. Ariga, Y. Lvov and G. Decher, Phys. Chem. Chem. Phys. **24** [7], 4097 (2021).

72) A. Yamamura, S. Watanabe, M. Uno, M. Mitani, C. Mitsui, J. Tsurumi, N. Isahaya, Y. Kanaoka, T. Okamoto and J. Takeya, Sci. Adv. **4** [2], eaao5758 (2018).

73) M. Ishii, Y. Yamashita, S. Watanabe, K. Ariga and J. Takeya, Nature **622** [7982], 285 (2023).

74) P. Mishra, J. P. Hill, S. Vijayaraghavan, W. V. Rossom, S. Yoshizawa, M. Grisolia, J. Echeverria, T. Ono, K. Ariga, T. Nakayama, C. Joachim and T. Uchihashi, Nano Lett. **15** [7], 4791 (2015).

75) D. Katsube, R. Shimizu, Y. Sugimoto, T. Hitosugi and M. Abe, Appl. Phys. Lett. **122** [7], 071602 (2023).

76) C. Rubia-Payá, G. de Miguel, M. T. Martín-Romero, J. J. Giner-Casares and L. Camacho, Adv. Colloid Interface Sci. **225**, 134 (2015).

77) N. Biswas, S. K. Bhattacharjee, C. Debnath, S. A. Hussain and D. Bhattacharjee, Phys. Scr. **98** [8], 085015 (2023).

78) M. Okuno, S. Yamada, T. Ohto, H. Tada, W. Nakanishi, K. Ariga and T. Ishibashi, J. Phys. Chem. Lett. **11** [7], 2422 (2020).

79) C. J. Moll, J. Versluis and H. J. Bakker, J. Phys. Chem. Lett. **12** [44], 10823 (2021).

80) T. Hasegawa, J. Phys. Chem. B **106** [16], 4112 (2002).

81) T. Hasegawa, Anal. Chem. **79** [12], 4385 (2007).

82) T. Hasegawa and N. Shioya, Bull. Chem. Soc. Jpn. **93** [9], 1127 (2020).

83) T. Hasegawa, *Quantitative Infrared Spectroscopy for Understanding of a Condensed Matter* (Springer, Tokyo, 2017).

84) V. P. Tolstoy, I. V. Chernyshova and V. A. Skryshevsky, *Handbook of Infrared Spectroscopy of Ultrathin Films* (2003).

85) T. Hasegawa, S. Takeda, A. Kawaguchi and J. Umemura, Langmuir **11** [4], 1236 (1995).

86) N. Shioya, S. Norimoto, N. Izumi, M. Hada, T. Shimoaka and T. Hasegawa, Appl. Spectrosc. **71** [5], 901 (2016).

87) N. Shioya, T. Shimoaka, R. Murdey and T. Hasegawa, Appl. Spectrosc. **71** [6], 1242 (2016).

88) N. Shioya, K. Tomita, T. Shimoaka and T. Hasegawa, J. Phys. Chem. A **123** [32], 7177 (2019).

89) R. Liu, W. Yang, W. Xu, J. Deng, C. Ding, Y. Guo, L. Zheng, J. Sun and M. Li, ACS Appl. Polym. Mater. **4** [4], 2233 (2022).

90) A. Hofmann, M. Schmid and W. Brütting, Adv. Opt. Mater. **9** [21], 2101004 (2021).

91) I. Osaka and K. Takimiya, Polymer **59**, A1 (2015).

92) D. Yokoyama, J. Mater. Chem. **21** [48], 19187 (2011).

93) N. Shioya, T. Shimoaka and T. Hasegawa, Chem. Lett. **43** [8], 1198 (2014).

94) N. Shioya, T. Shimoaka, K. Eda and T. Hasegawa, Phys. Chem. Chem. Phys. **17** [20], 13472 (2015).

95) N. SHIOYA, T. SHIMOAKA and T. HASEGAWA, Anal. Sci. **33** [1], 117 (2017).

96) N. Shioya, T. Shimoaka, K. Eda and T. Hasegawa, Macromolecules **50** [13], 5090 (2017).

97) K. Abiko and Y. Kato, Chem. Lett. **47** [3], 332 (2017).

98) M. Z. A. Aziz, K. Higashimine, N. Shioya, T. Shimoaka, T. Hasegawa, H. Sakai, V. Vohra and H. Murata, RSC Adv. **10** [61], 37529 (2020).

99) M. Hada, N. Shioya, T. Shimoaka, K. Eda, M. Hada and T. Hasegawa, Chem. A Eur. J. **22** [46], 16539 (2016).

100) K. Tomita, N. Shioya, R. Kise, T. Shimoaka, H. Yoshida, T. Koganezawa, K. Eda and T. Hasegawa, Thin Solid Films **665** [Appl. Phys. Lett. 86 2005], 85 (2018).

101) N. Shioya, M. Hada, T. Shimoaka, R. Murdey, K. Eda and T. Hasegawa, J. Phys. Chem. C **122** [8], 4540 (2018).

102) K. Tomita, N. Shioya, T. Shimoaka, K. Eda and T. Hasegawa, Bull. Chem. Soc. Jpn. **92** [8], 1335 (2019).

103) K. Tomita, N. Shioya, T. Shimoaka, K. K. Okudaira, H. Yoshida, T. Koganezawa and T. Hasegawa, Cryst. Growth Des. **21** [9], 5116 (2021).

104) K. Tomita, N. Shioya, T. Shimoaka, M. Wakioka and T. Hasegawa, Chem. Commun. **58** [13], 2116 (2022).

105) N. Shioya, R. Murdey, K. Nakao, H. Yoshida, T. Koganezawa, K. Eda, T. Shimoaka and T. Hasegawa, Sci. Rep. **9** [1], 579 (2019).

106) N. Shioya, R. Fujiwara, K. Tomita, T. Shimoaka and T. Hasegawa, J. Phys. Chem. A **124** [13], 2714 (2020).

107) N. Shioya, R. Fujiwara, K. Tomita, T. Shimoaka, K. K. Okudaira, H. Yoshida, T. Koganezawa and T. Hasegawa, J. Phys. Chem. C **125** [4], 2437 (2021).

108) S. Nagai, Y. Inaba, T. Nishi, H. Kobayashi and S. Tomiya, Phys. Rev. Mater. **5** [1], 013801 (2021).

109) S. Nagai, Y. Inaba, T. Nishi and S. Tomiya, Appl. Phys. Express **15** [1], 015502 (2022).

110) T. Nakamura, N. Shioya, T. Shimoaka, R. Nishikubo, T. Hasegawa, A. Saeki, Y. Murata, R. Murdey and A. Wakamiya, Chem. Mater. **31** [5], 1729 (2019).

111) T. Nakamura, N. Shioya, T. Hasegawa, Y. Murata, R. Murdey and A. Wakamiya, ChemPlusChem **84** [9], 1396 (2019).

112) M. A. Truong, J. Lee, T. Nakamura, J. Seo, M. Jung, M. Ozaki, A. Shimazaki, N. Shioya, T. Hasegawa, Y. Murata, S. M. Zakeeruddin, M. Grätzel, R. Murdey and A. Wakamiya, Chem. A Eur. J. **25** [27], 6741 (2019).

113) A. Sugie, W. Han, N. Shioya, T. Hasegawa and H. Yoshida, J. Phys. Chem. C **124** [18], 9765 (2020).

114) S. Nagamatsu and S. S. Pandey, Sci. Rep. **10** [1], 20020 (2020).

115) N. Shioya, M. Yoshida, M. Fujii, T. Shimoaka, R. Miura, S. Maruyama and T. Hasegawa, J. Phys. Chem. Lett. **13** [51], 11918 (2022).

116) T. Shimoaka, Y. Yamaguchi, N. Shioya, A. Ajayaghosh, T. Mori, K. Ariga and T. Hasegawa, J. Phys. Chem. C **127** [19], 9336 (2023).

117) R. Ruiz, D. Choudhary, B. Nickel, T. Toccoli, K.-C. Chang, A. C. Mayer, P. Clancy, J. M. Blakely, R. L. Headrick, S. Iannotta and G. G. Malliaras, Chem. Mater. **16** [23], 4497 (2004).

118) D. Knipp, R. A. Street, A. Völkel and J. Ho, J. Appl. Phys. **93** [1], 347 (2003).

119) C. D. Dimitrakopoulos and P. R. L. Malenfant, Adv. Mater. **14** [2], 99 (2002).

120) D. J. Gundlach, Y. Y. Lin, T. N. Jackson, S. F. Nelson and D. G. Schlom, IEEE Electron Device Lett. **18** [3], 87 (1997).

121) C. D. Dimitrakopoulos, A. R. Brown and A. Pomp, J. Appl. Phys. **80** [4], 2501 (1996).

122) T. Minakata, H. Imai and M. Ozaki, J. Appl. Phys. **72** [9], 4178 (1992).

123) K. O. Lee and T. T. Gan, Chem. Phys. Lett. **51** [1], 120 (1977).

124) Y. Kamura, I. Shirotani, H. Inokuchi and Y. Maruyama, Chem. Lett. **3** [6], 627 (2006).

125) J. Yang, D. Yan and T. S. Jones, Chem. Rev. **115** [11], 5570 (2015).

126) H. Iino, T. Usui and J. Hanna, Nat. Commun. **6** [1], 6828 (2015).

127) S. Hofer, A. Hofer, J. Simbrunner, M. Ramsey, M. Sterrer, A. Sanzone, L. Beverina, Y. Geerts and R. Resel, J. Phys. Chem. C **125** [51], 28039 (2021).

128) H. Minemawari, J. Tsutsumi, S. Inoue, T. Yamada, R. Kumai and T. Hasegawa, Appl. Phys. Express **7** [9], 091601 (2014).

129) S. Hofer, W. Bodlos, J. Novák, A. Sanzone, L. Beverina and R. Resel, Liq. Cryst. **48** [13], 1888 (2021).

130) J. Umemura, T. Kamata, T. Kawai and T. Takenaka, J. Phys. Chem. **94** [1], 62 (1990).

131) H. Hoffmann, U. Mayer and A. Krischanitz, Langmuir **11** [4], 1304 (1995).

132) R. Mendelsohn, G. Mao and C. R. Flach, Biochim. Biophys. Acta (BBA) - Biomembr. **1798** [4], 788 (2010).

133) J. Hanna, A. Ohno and H. Iino, Thin Solid Films **554**, 58 (2014).

134) N. Shioya, M. Fujii, T. Shimoaka, K. Eda and T. Hasegawa, Sci. Rep. **12** [1], 4448 (2022).

135) K. Shimada, S. Maruyama, T. Miyadera, K. Kaminaga and Y. Matsumoto, ACS Appl. Mater. Interfaces **15** [38], 45411 (2023).

136) N. Shioya, T. Fang, M. Fujii, R. Fujiwara, H. Hayashi, H. Yamada and T. Hasegawa, Langmuir **40** [1], 1137 (2024).

137) A. Afzali, C. D. Dimitrakopoulos and T. L. Breen, J. Am. Chem. Soc. **124** [30], 8812 (2002).

138) A. Hamaguchi, T. Negishi, Y. Kimura, Y. Ikeda, K. Takimiya, S. Z. Bisri, Y. Iwasa and T. Shiro, Adv. Mater. **27** [42], 6606 (2015).

139) Y. Kimura, T. Nagase, T. Kobayashi, A. Hamaguchi, Y. Ikeda, T. Shiro, K. Takimiya and H. Naito, Adv. Mater. **27** [4], 727 (2015).

140) S. Yaginuma, K. Itaka, M. Haemori, M. Katayama, K. Ueno, T. Ohnishi, M. Lippmaa, Y. Matsumoto and H. Koinuma, Appl. Phys. Express **1** [1], 015005 (2008).

141) T. Miyadera, T. Sugita, H. Tampo, K. Matsubara and M. Chikamatsu, ACS Appl. Mater. Interfaces **8** [39], 26013 (2016).

142) O. Teschke and E. F. de Souza, Chem. Phys. Lett. **403** [1–3], 95 (2005).

143) D. Jiang, K. L. Dinh, T. C. Ruthenburg, Y. Zhang, L. Su, D. P. Land and F. Zhou, J. Phys. Chem. B **113** [10], 3160 (2009).

144) K. Ariga, Anal. Sci. **32** [11], 1141 (2016).

145) T. Hasegawa, L. Matsumoto, S. Kitamura, S. Amino, S. Katada and J. Nishijo, Anal. Chem. **74** [23], 6049 (2002).

146) T. HASEGAWA, G. ARAI, K. KASAMATSU, H. KAKUDA and Y. ISHII, Int. J. Soc. Mater. Eng. Resour. **12** [1], 22 (2004).

147) T. Hasegawa, Y. Nakano and Y. Ishii, Anal. Chem. **78** [6], 1739 (2006).

148) T. Hasegawa, Y. Iiduka, H. Kakuda and T. Okada, Anal. Chem. **78** [17], 6121 (2006).

149) T. Hasegawa, Y. Itoh and A. Kasuya, Anal. Sci. **24** [1], 105 (2008).

150) T. Hasegawa, H. Kakuda and N. Yamada, J. Phys. Chem. B **109** [10], 4783 (2005).

151) T. Hasegawa, D. Moriya, H. Kakuda, C. Li, J. Orbulescu and R. M. Leblanc, J. Phys. Chem. B **109** [26], 12856 (2005).

152) T. Hasegawa, Y. Sato, T. Okada, M. Shibukawa, C. Li, J. Orbulescu and R. M. Leblanc, J. Phys. Chem. B **111** [51], 14227 (2007).

153) M. G. Spillantini, M. L. Schmidt, V. M.-Y. Lee, J. Q. Trojanowski, R. Jakes and M. Goedert, Nature **388** [6645], 839 (1997).

154) M. G. Spillantini, R. A. Crowther, R. Jakes, M. Hasegawa and M. Goedert, Proc. Natl. Acad. Sci. **95** [11], 6469 (1998).

155) J. A. Wright and D. R. Brown, J. Neurosci. Res. **86** [3], 496 (2008).

156) E. Dalfó and I. Ferrer, Neurobiol. Aging **29** [3], 408 (2008).

157) C. Wang, S. K. Sharma, O. S. Olaluwoye, S. A. Alrashdi, T. Hasegawa and R. M. Leblanc, Colloids Surf. B: Biointerfaces **183**, 110401 (2019).

158) C. Wang, Y. Zhou, C. Ewuola, T. Akinleye, T. Hasegawa and R. M. Leblanc, Anal. Sci. **38** [7], 935 (2022).

159) Z. Qin, D. Hu, S. Han, D.-P. Hong and A. L. Fink, Biochemistry **46** [46], 13322 (2007).

160) C. Wang, N. Shah, G. Thakur, F. Zhou and R. M. Leblanc, Chem. Commun. **46** [36], 6702 (2010).

161) S. M. Decatur, Acc. Chem. Res. **39** [3], 169 (2006).

162) S. Li, J. D. Combs, O. E. Alharbi, J. Kong, C. Wang and R. M. Leblanc, Chem. Commun. **51** [63], 12537 (2015).

163) R. Ishige, K. Tanaka and S. Ando, Macromol. Chem. Phys. **219** [3], 1700370 (2018).

164) R. Ishige, K. Tanaka and S. Ando, Polym. J. **53** [5], 603 (2021).

165) R. Imanishi, Y. Nagashima, M. Hara, S. Nagano and T. Seki, Chem. Lett. **48** [2], 98 (2018).

166) K. W. Lee, Macromolecules **29**, 8894 (1996).

167) J. A. Castellano, Mol. Cryst. Liq. Cryst. **94** [1–2], 33 (1983).

168) Y. Morikawa, T. Kondo, S. Nagano and T. Seki, Chem. Mater. **19** [7], 1540 (2007).

169) T. Uekusa, S. Nagano and T. Seki, Macromolecules **42** [1], 312 (2009).

170) K. Fukuhara, Y. Fujii, Y. Nagashima, M. Hara, S. Nagano and T. Seki, Angew. Chem. Int. Ed. **52** [23], 5988 (2013).

171) D. Tanaka, Y. Nagashima, M. Hara, S. Nagano and T. Seki, Langmuir **31** [42], 11379 (2015).

172) T. Hama and N. Watanabe, Chem. Rev. **113** [12], 8783 (2013).

173) T. Hama, A. Ishibashi, A. Kouchi, N. Watanabe, N. Shioya, T. Shimoaka and T. Hasegawa, J. Phys. Chem. Lett. **11** [18], 7857 (2020).

174) T. Nagasawa, R. Sato, T. Hasegawa, N. Numadate, N. Shioya, T. Shimoaka, T. Hasegawa and T. Hama, Astrophys. J. Lett. **923** [1], L3 (2021).

175) T. Nagasawa, N. Numadate and T. Hama, J. Raman Spectrosc. **53** [10], 1748 (2022).

176) A. C. A. Boogert, A. G. G. M. Tielens, C. Ceccarelli, A. M. S. Boonman, E. F. van Dishoeck, J. V. Keane, D. C. B. Whittet and T. de Graauw, arXiv **360**, 683 (2000).

177) A. G. G. M. Tielens, Rev. Mod. Phys. **85** [3], 1021 (2013).

178) R. Balog, P. Cicman, N. C. Jones and D. Field, Phys. Rev. Lett. **102** [7], 073003 (2009).

179) O. Plekan, A. Cassidy, R. Balog, N. C. Jones and D. Field, Phys. Chem. Chem. Phys. **13** [47], 21035 (2011).

180) D. Field, O. Plekan, A. Cassidy, R. Balog, N. C. Jones and J. Dunger, Int. Rev. Phys. Chem. **32** [3], 345 (2013).

181) K. Kutzner, Thin Solid Films **14** [1], 49 (1972).

182) J. Chrzanowski and B. Sujak, Thin Solid Films **79** [2], 101 (1981).

183) W. L. Barnes, J. Susskind, R. H. Hunt and E. K. Plyler, J. Chem. Phys. **56** [10], 5160 (1972).

184) S. Nakajima, Y. Toyozawa and R. Abe, *The Physics of Elementary Excitations* (Springer Berlin, Heidelberg, 2011).

185) C. Kittel, *Introduction To Solid State Physics (8th Ed.)* (Wiley, 2005).

186) R. L. Hudson, M. J. Loeffler and P. A. Gerakines, J. Chem. Phys. **146** [2], 024304 (2017).

187) M. A. Ovchinnikov and C. A. Wight, J. Chem. Phys. **102** [1], 67 (1995).

188) J. Lasne, A. Rosu-Finsen, A. Cassidy, M. R. S. McCoustra and D. Field, Phys. Chem. Chem. Phys. **17** [32], 20971 (2015).

189) O. Plekan, A. Rosu-Finsen, A. M. Cassidy, J. Lasne, M. R. S. McCoustra and D. Field, Eur. Phys. J. D **71** [6], 162 (2017).

190) X. L. Chen and R. N. Sudan, AIP Conf. Proc. **318**, 34 (1994).

191) G. Junk and H. J. Svec, Geochim. Cosmochim. Acta **14** [3], 234 (1958).

192) V. Buch and J. P. Devlin, J. Chem. Phys. **94** [5], 4091 (1991).

193) J. A. Noble, E. Michoulier, C. Aupetit and J. Mascetti, Astron. Astrophys. **644**, A22 (2020).

194) J. He, A. R. Clements, S. Emtiaz, F. Toriello, R. T. Garrod and G. Vidali, Astrophys. J. **878** [2], 94 (2019).

195) H. Kakuda, T. Hasegawa, T. Tanaka, K. Tanaka and M. Shionoya, Chem. Phys. Lett. **415** [1–3], 172 (2005).

196) K. P. Stevenson, G. A. Kimmel, Z. Dohnálek, R. S. Smith and B. D. Kay, Science **283** [5407], 1505 (1999).

197) R. Yamaguchi, T. Hosomi, M. Otani, K. Nagashima, T. Takahashi, G. Zhang, M. Kanai, H. Masai, J. Terao and T. Yanagida, Langmuir **37** [17], 5172 (2021).

198) N. Barsan, D. Koziej and U. Weimar, Sens. Actuators B: Chem. **121** [1], 18 (2007).

199) A. Mirzaei, S. G. Leonardi and G. Neri, Ceram. Int. **42** [14], 15119 (2016).

200) C. Wang, T. Hosomi, K. Nagashima, T. Takahashi, G. Zhang, M. Kanai, H. Zeng, W. Mizukami, N. Shioya, T. Shimoaka, T. Tamaoka, H. Yoshida, S. Takeda, T. Yasui, Y. Baba, Y. Aoki, J. Terao, T. Hasegawa and T. Yanagida, Nano Lett. **19** [4], 2443 (2019).

201) P. Fuchs, C. Loeseken, J. K. Schubert and W. Miekisch, Int. J. Cancer **126** [11], 2663 (2010).

202) D. Poli, M. Goldoni, M. Corradi, O. Acampa, P. Carbognani, E. Internullo, A. Casalini and A. Mutti, J. Chromatogr. B **878** [27], 2643 (2010).

203) J. Huang, S. Kumar and G. B. Hanna, J. Breath Res. **8** [3], 037104 (2014).

204) K. Hadjiivanov, Adv. Catal. **57**, 99 (2014).

205) R. R. Gay, M. H. Nodine, V. E. Henrich, H. J. Zeiger and E. I. Solomon, J. Am. Chem. Soc. **102** [22], 6752 (1980).

206) A. Yokoi, M. Ukai, T. Yasui, Y. Inokuma, K. Hyeon-Deuk, J. Matsuzaki, K. Yoshida, M. Kitagawa, K. Chattrairat, M. Iida, T. Shimada, Y. Manabe, I.-Y. Chang, E. Asano-Inami, Y. Koya, A. Nawa, K. Nakamura, T. Kiyono, T. Kato, A. Hirakawa, Y. Yoshioka, T. Ochiya, T. Hasegawa, Y. Baba, Y. Yamamoto and H. Kajiyama, Sci. Adv. **9** [27], eade6958 (2023).

207) M. Uesaka, Y. Saito, S. Yoshioka, Y. Domoto, M. Fujita and Y. Inokuma, Commun. Chem. **1** [1], 23 (2018).

208) Y. Manabe, M. Uesaka, T. Yoneda and Y. Inokuma, J. Org. Chem. **84** [16], 9957 (2019).

209) T. Hasegawa, A. Nakagawara, T. Takagi, T. Shimoaka, N. Shioya and M. Sonoyama, J. Chem. Phys. **160** [6], 064704 (2024).

210) D. W. Berreman, Phys. Rev. **130** [6], 2193 (1963).

211) N. Nagai, M. Okawara and Y. Kijima, Appl. Spectrosc. **70** [8], 1278 (2015).

212) A. Fukumi, T. Shimoaka, N. Shioya, N. Nagai and T. Hasegawa, J. Chem. Phys. **153** [4], 044703 (2020).

213) T. Hasegawa, Chem. Rec. **17** [10], 903 (2017).

214) T. Hasegawa, T. Shimoaka, N. Shioya, K. Morita, M. Sonoyama, T. Takagi and T. Kanamori, ChemPlusChem **79** [10], 1421 (2014).

215) K. Honda, M. Morita, H. Otsuka and A. Takahara, Macromolecules **38** [13], 5699 (2005).